JGR Planets

RESEARCH ARTICLE
10.1029/2022JE007522

Special Section:
The Mars Perseverance Rover Jezero Crater Floor Campaign

This article is a companion to Viúdez-Moreiras et al. (2022), https://doi.org/10.1029/2022JE007523.

Key Points:

- A mostly repeatable diurnal cycle of winds is consistent with primary control by regional and local slope flows
- Great sub-diurnal and sol-to-sol variability in winds was observed during the calm period at night
- Traveling and gravity waves were observed, along with the probable effect of enhanced tidal flows

Correspondence to:
D. Viúdez-Moreiras,
viudezmd@inta.es;
viudezmd@cab.inta-csic.es

Citation:
Viúdez-Moreiras, D., Lemmon, M., Newman, C. E., Guzewich, S., Mischna, M., Gómez-Elvira, J., et al. (2022). Winds at the Mars 2020 landing site: 1. Near-surface wind patterns at Jezero crater. *Journal of Geophysical Research: Planets*, *127*, e2022JE007522. https://doi.org/10.1029/2022JE007522

Received 8 AUG 2022
Accepted 22 NOV 2022

Winds at the Mars 2020 Landing Site: 1. Near-Surface Wind Patterns at Jezero Crater

D. Viúdez-Moreiras[1], M. Lemmon[2], C. E. Newman[3], S. Guzewich[4], M. Mischna[5], J. Gómez-Elvira[6], K. Herkenhoff[7], A. Sánchez-Lavega[8], M. de la Torre[5], J. A. Rodríguez-Manfredi[1], R. D. Lorenz[9], J. Pla-García[1], R. Hueso[7], M. Richardson[3], L. Tamppari[5], M. Smith[4], V. Apéstigue[6], D. Toledo[6], and J. Bell[10]

[1]Centro de Astrobiologia (CAB, CSIC-INTA) and National Institute for Aerospace Technology (INTA), Madrid, Spain, [2]Space Science Institute, College Station, TX, USA, [3]Aeolis Research, Chandler, AZ, USA, [4]NASA Goddard Spaceflight Center, Greenbelt, MD, USA, [5]Jet Propulsion Laboratory, California Institute of Technology, Pasadena, CA, USA, [6]National Institute for Aerospace Technology (INTA), Madrid, Spain, [7]USGS Astrogeology Science Center, Flagstaff, AZ, USA, [8]Universidad del País Vasco (UPV/EHU), Bilbao, Spain, [9]Johns Hopkins University Applied Physics Laboratory, Laurel, MD, USA, [10]School of Earth and Space Exploration, Arizona State University, Tempe, AZ, USA

Abstract This is the first part of a two-part paper. NASA's Mars 2020 Perseverance rover measured winds on the Jezero crater floor close to the delta of an ancient river. A mostly repeatable diurnal cycle was observed and presented two regimes: (a) a convective regime, from dawn to sunset, with average easterly to southeasterly winds, during which maximum wind speeds were measured, and (b) a nighttime regime with westerly-northwesterly winds followed by a relatively calm period with highly variable wind directions as a function of sol and time of night. The timing and magnitude of the observed regimes are consistent with primary control by regional and local slope flows. Data suggest that the surface circulation at Jezero region in northern spring and summer is highly unaffected by large-scale circulation except during particular periods in the diurnal cycle or generally during dust storms, which is supported by MarsWRF model simulations. Consequently, the observed seasonal variability was weak. However, sol-to-sol and seasonal variability were measured, most of it during certain nighttime periods. Traveling waves consistent with baroclinic instability were clearly observed in surface winds at $L_s \sim 75°$. The early MY36/2022A regional dust storm at $L_s \sim 153°$ disturbed the wind patterns with changes suggesting enhanced tidal flows. After sunset, the dust storm also produced detectable gravity wave activity, increasing the mixing in the nighttime planetary boundary layer during storm conditions. Inferred wind directions from dust devil movies strongly suggest that prevailing winds continued to be slope-driven during the late summer, fall and early winter seasons.

Plain Language Summary This is the first part of a two-part paper. NASA's Mars 2020 Perseverance rover landed close to the western rim of Jezero crater (18.44°N, 77.45°E) on 18 February 2021. The wind data acquired by the rover measured a mostly repeatable diurnal cycle with two regimes: (a) a convective period, from dawn to sunset with average easterly to southeasterly winds, in which maximum wind speeds were measured, and (b) a nighttime regime with westerly-northwesterly winds followed by a relatively calm period with highly variable wind directions as a function of sol and time of night. The timing and magnitude of the observed regimes are consistent with primary control by regional and local slope flows, as have been observed to varying degrees at other landing sites on Mars. Data suggest that the surface circulation at Jezero is highly unaffected by large-scale circulation, except during particular periods. An early regional dust storm prior to fall equinox also disturbed wind patterns with changes suggesting the strengthening of flows linked to large-scale atmospheric oscillations called tides. The latter are primarily driven by the daily pattern of solar heating around Mars and its interaction with topography.

1. Introduction

NASA's Mars 2020 Perseverance rover successfully landed close to the western rim of Jezero crater (18.44°N, 77.45°E) on 18 February 2021 (areocentric solar longitude, $L_s \sim 5°$). The rover is seeking signs of potential ancient life on Mars and preparing, for the first time, a set of samples for possible return to Earth (Farley et al., 2020). Among the mission objectives, Mars 2020 should enable future Mars exploration focused on manned missions with a characterization of the atmospheric environment. To fulfill this requirement, the Mars Environmental

Dynamics Analyzer (MEDA) instrument (Rodríguez-Manfredi et al., 2021) on board Perseverance rover includes a wind sensor (WS) that combines with other meteorological measurements to allow the characterization of the atmospheric environment of Jezero crater and obtain insight into the processes that drive the Martian atmosphere.

Near-surface winds are a key mechanism for the exchange of heat, mass, and momentum between the surface and the atmosphere. On Mars, suspended dust in the atmosphere is a significant driver of weather and climate. Therefore, comprehensive knowledge of the surface wind patterns is desirable to fully understand the weather and climate of the planet as well as how dust storms originate and develop. To date, however, few missions have measured the surface winds on Mars, and their measurement has been complex and sometimes constrained by instrumentation issues. The first measurements of the Martian winds were taken by the Viking Landers (VLs) in the 1970s at 22.5°N 48°W (VL-1) and at 48°N 134°E (VL-2). Those missions observed light winds of a few meters per second with a marked rotation in the diurnal cycle. They also reported dramatic changes as a function of season and in the presence of dust events (Ryan & Henry, 1979; Ryan et al., 1978), which were attributed to variable regional slope flows, diurnally varying planetary boundary layer (PBL) coupling, large-scale circulation, thermal tides and baroclinic waves (Barnes, 1980; Hess et al., 1977; Murphy et al., 1990; Ryan et al., 1978).

Twenty years later, the Mars Pathfinder mission again measured Martian surface winds. The Pathfinder lander acquired sparse wind data during several sols and enabled the first direct measurements of near-surface wind profiles on Mars, including a determination of aerodynamic roughness length and wind friction speeds (Sullivan et al., 2000). Later, the Phoenix lander measured winds (Holstein-Rathlou et al., 2010) in the polar region (68.2°N, 125.8°W) and at various heights during ~150 mission sols, showing highly variable diurnal conditions due to the daytime convective turbulence and reporting wind patterns possibly driven by thermal tides and weather systems. The Mars Science Laboratory (MSL) measured surface winds at Gale crater, but the retrieval presented problems due to damage to the WS during MSL's landing. A comprehensive diurnal and seasonal surface wind characterization was presented covering the two Mars years over which the WS operated in the northwest crater floor and on the northwestern slopes of Aeolis Mons. Wind data showed that the patterns at Gale crater are driven mostly by local slope winds on Aeolis Mons in accordance with mesoscale model predictions (Newman et al., 2017; Pla-Garcia et al., 2016; Rafkin et al., 2016; Tyler & Barnes, 2013; Viúdez-Moreiras et al., 2019a, 2019b). To date, these wind patterns are the most complex ever seen on Mars due to strong constructive and destructive interactions between different scales variably affecting the near-surface atmosphere in the crater. Wind-driven erosion signatures and sand transport have also been repeatedly observed by the mission (e.g., Schieber et al., 2020; Sullivan & Kok, 2017; Vasavada, 2022, and references therein). Local winds in Gale crater have been proposed to drive the abundance of methane detected by MSL near the surface and could even induce advective flows in the regolith (e.g., Etiope & Oehler, 2019; Viúdez-Moreiras, 2021; Viúdez-Moreiras, Arvidson, et al., 2020; Webster et al., 2018).

InSight landed in Elysium Planitia (~4.5°N, 136°E) right after the decay of the MY34/2018 Global Dust Storm and before the onset of the MY34/2019 Large Dust Storm (LDS) (e.g., Montabone et al., 2020). Before and after the storm began, the observed wind patterns resulted from the interaction between regional and local slope flows induced by topography, together producing a diurnal perturbation superimposed on a mean flow, dominated by the Hadley cell but with modifications due to channeling effects from the regional topography (Banfield et al., 2020; Viúdez-Moreiras, Newman, et al., 2020). Pressure tides were strongly affected by the LDS and produced a dramatic change in the wind patterns that were attributed to enhanced tidal flows. Also, baroclinic wave signatures were observed in the data. InSight's surface wind measurements have also been crucial for aeolian studies. Aeolian changes at InSight's landing site in Elysium Planitia were infrequent and probably primarily driven by high wind speeds inside convective vortices (Charalambous et al., 2021). The effect of ambient wind speeds on convective vortex encounters was also observed (Spiga et al., 2021), and wind measurements inside vortices were reported, complementing those observed by MSL (Banfield et al., 2020; Kahanpää & Viúdez-Moreiras, 2021; Spiga et al., 2021).

Mars 2020 has detected a rich dynamic atmosphere and aeolian environment in Jezero crater with dust lifting mainly produced by the passage of convective vortices and convection cells (Bell et al., 2022; Newman et al., 2022). Measurements obtained during the first few sols of the mission suggested that wind patterns are mainly controlled by regional and local slope flows in accordance with pre-landing model simulations (e.g., Newman et al., 2021). Perseverance also characterized an early MY36/2022A regional dust storm (RDS) in January 2022, which produced several dust-lifting events (Lemmon et al., 2022). The strong aeolian activity present at

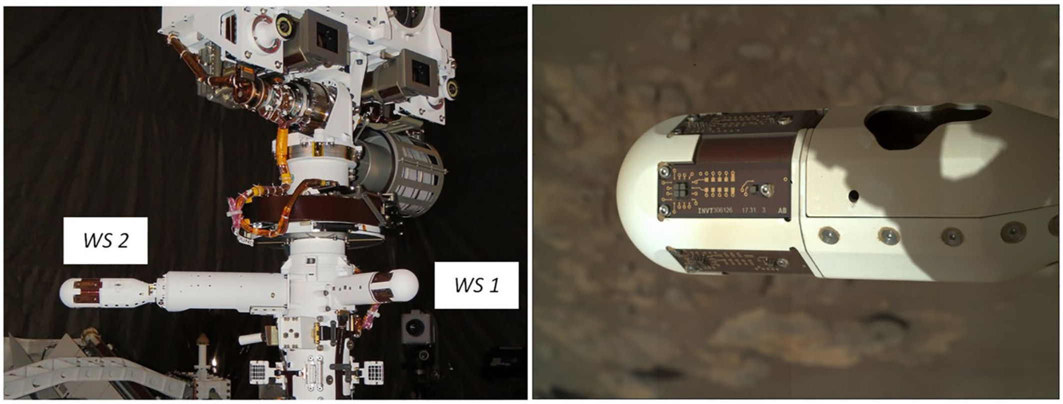

Figure 1. (Left) Mars Environmental Dynamics Analyzer (MEDA) wind sensor booms (WS1 and WS2) on Mars 2020 Perseverance's Remote Sensing Mast (right) MEDA WS2 captured on the Martian surface by the SHERLOC WATSON camera, onboard Perseverance, as part of the study performed after the event on sol 313 ($L_s \sim 152°$). Credit: NASA/JPL-Caltech.

Jezero has had side effects on the instrumentation. The Mars 2020 WS has been systematically damaged throughout the mission, although efforts are being made to partially recover most of the functionality. Furthermore, Mars 2020 has deployed, for the first time, an unmanned aerial vehicle on another planet, the Ingenuity helicopter (Balaram et al., 2021; Farley et al., 2020), whose safety is strongly dependent on atmospheric conditions. Together with the InSight's WS, the Mars 2020 WS is currently operating on the Martian surface.

In this two-part paper, we present the winds at the Mars 2020 landing site on the Jezero crater floor acquired in northern spring and summer. This part focuses on the Mars 2020 MEDA wind measurements, describing the mechanisms that may be involved in the near-surface wind patterns at Jezero and presenting the observed winds throughout the mission from the diurnal to the seasonal scales, including the effects of the MY36/2022A RDS on the near-surface circulation at Jezero. We use MarsWRF General Circulation Model (GCM) to support the potential influence of particular mechanisms into the near-surface winds. The second part presents the observed wind variability focusing on the sub-diurnal scale. This first part is structured as follows: Section 2 describes the MEDA WS observations and the support that the wind measurements are able to provide for Ingenuity and future helicopters on Mars. Section 3 introduces the mechanisms that may affect the near-surface wind patterns at Jezero crater. Section 4 shows the diurnal cycle of winds at Jezero, and describes the sol-to-sol and seasonal cycle for the period covered by the sensor. Section 6 presents the effects of the MY36/2022A RDS. Finally, Section 7 presents the conclusions.

2. Methods: The Mars 2020 MEDA Wind Sensor and Observations

2.1. The Mars 2020 MEDA Wind Sensor

The Mars 2020 MEDA WS consists of two booms (WS1 and WS2) angled at 120° to each other and mounted on the Perseverance's Remote Sensing Mast (RSM) as shown in Figure 1. WS1 points to the direction of the rover movement with a displacement of 6° in azimuth (Rodríguez-Manfredi et al., 2021) with the WS2 rotated 120° clockwise to the WS1. The WS measures winds by thermal anemometry, as in the VLs, MSL, and InSight WS (Banfield et al., 2020; Gómez-Elvira et al., 2012; Hess et al., 1977), using thin-film resistors patterned on the surface of a silicon chip. Placed at 1.5 m above the ground, each boom has six sensor boards angled differently to the incoming wind direction in different planes. The six sensor boards included on each boom allow for substantial redundancy in wind retrieval and enable accurate measurement of vertical winds, significantly improving the preceding designs implemented in the MSL and in the InSight WSs.

As in previous missions, the measured winds can be affected by the rover or platform itself, that is, the ambient winds can be perturbed by the presence of the rover and thus the measured winds could differ from the ambient winds. The Perseverance rover is mostly similar to the MSL Curiosity rover in terms of both the platform and in the sensor allocation with the RSM being the main source of perturbation. The position of the booms allows for the selection of the best boom for an incoming wind direction. On MSL, based on thorough CFD modeling and examination of REMS wind measurements after the sensor damage during MSL's landing, accurate wind speeds and directions were retrieved only for winds coming from the front boom hemisphere with incident wind angles between −90° and +90° relative to the boom (Gómez-Elvira et al., 2012; Viúdez-Moreiras et al., 2019a). Perseverance WS2 was designed to minimize the RSM perturbation and other disturbances by using a larger WS2 boom (393 vs. 170 mm). Allocation and mechanical constraints on the Perseverance rover to be experienced during the cruise stage prevented the inclusion of a fixed WS2, which led to the development of a deployable boom once on the Martian surface. Thus, the sensors are farther from the RSM, allowing wider incident angles to be retrieved, particularly those of the WS2 boom, thus strongly minimizing the uncertainties in the rear hemisphere of the rover. Individual wind speeds and directions were estimated at each boom from all six sensor boards based on a wind tunnel calibration database augmented by CFD modeling, correcting potential disturbances from the RSM and its appendages, and combined according to the incident wind direction.

Mars 2020 wind data incorporate a relatively new issue that must be considered. The radioisotope thermoelectric generator (RTG) generates a thermal plume that could perturb the flow toward the sensors if the incoming wind direction comes from the rover's rear hemisphere. This thermal disturbance was not involved in the MSL REMS data, given that only the front pointing WS boom was available to retrieve winds due to the damage on the rear boom at MSL's landing. The RTG can provoke disturbances in the wind measurements, mainly in wind speeds. Thus, winds coming from the rear angles close to the RTG were not considered in this study. Fortunately, as in MSL, the rover moves regularly, so the attitude changes accordingly and the winds are sampled from every direction throughout the mission, despite gaps that are present if the rover is placed for long time at the same attitude.

MEDA WS can characterize the horizontal component of the wind at the sensor location with a resolution of at least in the speed of 0.5 ms^{-1} in the 0–10 ms^{-1} range and of 1 ms^{-1} for wind speeds above 10 ms^{-1} up to 40 ms^{-1}. The performance decreases for temperatures greater than 223 K, reaching a resolution of 1.25 ms^{-1} at 293 K.

2.2. The Mars 2020 Wind Measurements and Observations

The MEDA instrument performed sparse measurements beginning with sol 1 ($L_s \sim 5°$), and starting systematic operations on sol 28 ($L_s \sim 18°$, Figure 2). The MEDA WS2 was deployed on sol 10 (28 February 2021). Discrepancies in the obtained results on Mars and the malfunction of a sensor board on WS2 delayed the start of WS operations to sol 36 ($L_s \sim 22°$). Mars 2020 operational constraints limited the measurements in the first sols, focusing the observations on supporting the Ingenuity helicopter flights, particularly to select the best time of the day to minimize the risks for the first flights. The primary helicopter campaign concluded on sol 75 ($L_s \sim 41°$), thus starting nominal wind observations, including further coverage of morning, night-fall, and nighttime since then. MEDA measurements were acquired for even or odd Martian hours, alternatively, from sol to sol, in Martian local mean solar time (LMST). In addition to these background hourly measurements, other blocks may be included in each plan considering the operational constraints of the Perseverance rover. Although not usually applied in the first mission sols to simplify the complex surface operations, the background measurements may be moved in time and enlarged or shortened if necessary. A potential issue between the WS and the antenna of the rover meant that the WS had to be turned off during the ultra-high frequency communication passes of the satellites, thus losing those wind observations while MEDA continued acquiring data with the remaining sensors.

Given the high sub-diurnal, diurnal, and intersol variability inherent in winds, this sampling, together with significant gaps due to the satellite passes, prevented proper characterization of certain features in the wind data. Measurement cadence was increased at sol 281 ($L_s \sim 136°$) after optimizing wind observations in the Mars 2020 tactical plans. The arrival of the MY36/2022A RDS (see Section 6) led to the activation of the dust storm campaign on sol 311 ($L_s \sim 151°$, Figure 2) with continuous observations along several hours, significantly enhancing the wind data over those sols. Observations began at a 2 Hz sampling frequency, lowered to 1 Hz after sol 152, due to the need to extend the observation times while maintaining the operational constraints on data volume.

Flying debris both lofted by the winds and produced during the descent of spacecraft is known to damage instrumentation in the severe conditions present on the Martian surface. MSL REMS WS was damaged during MSL's landing due to flying debris making one of the two sensor booms inoperative. Dust aerosol impacts occurring due to the strong winds observed during the latest operational period of the sensor (around the southern spring equinox while approaching Aeolis Mons) are likely responsible for the final REMS WS sensor failure on MSL

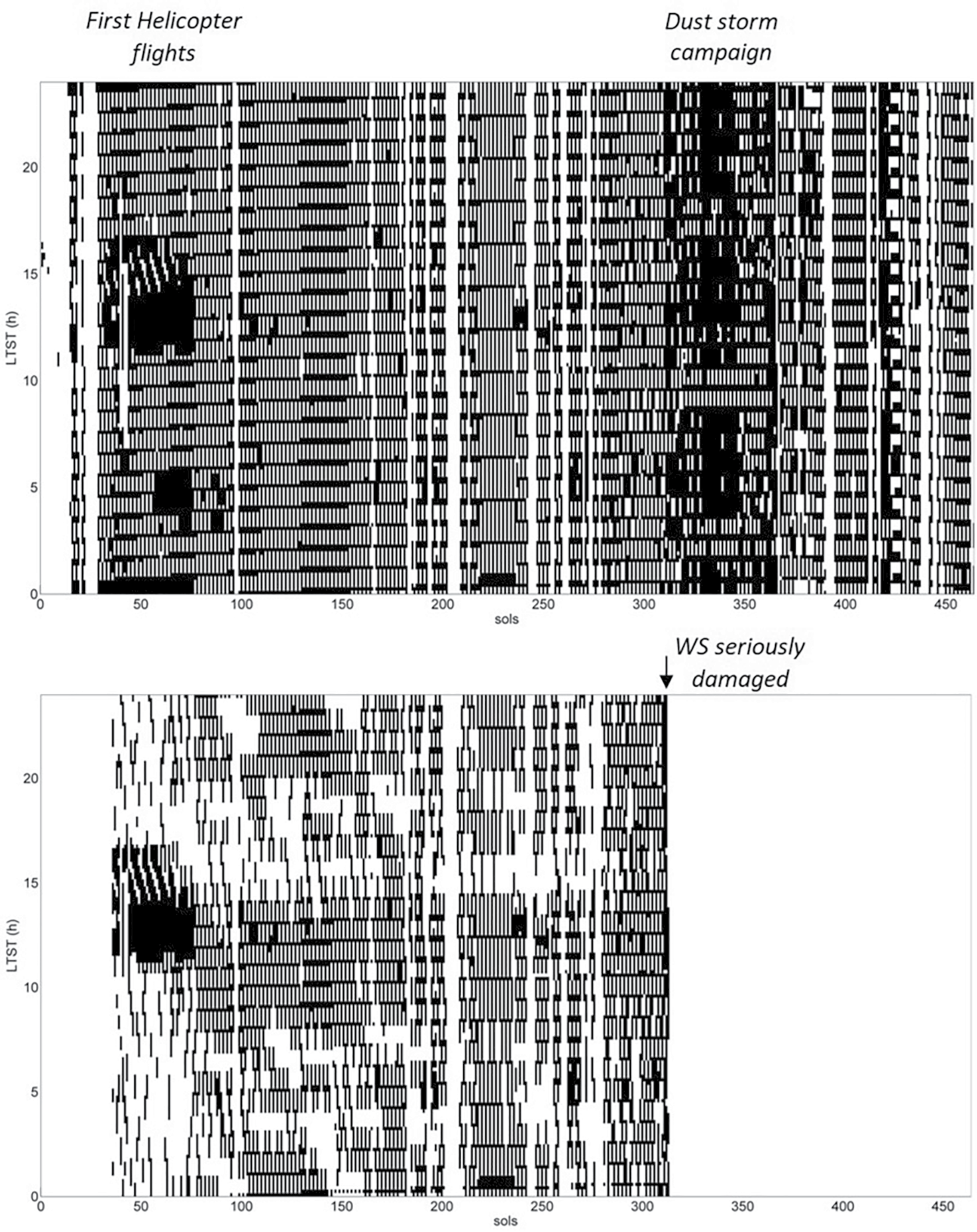

Figure 2. (Top) Mars Environmental Dynamics Analyzer (MEDA) instrument observations performed until sol 450 ($L_s \sim 233°$), as a function of local true solar time (LTST), showed as black areas. The special campaigns to support the first helicopter flights (sol 28–75, $L_s \sim 18°–41°$) and to widely cover the 2022/MY36A regional dust storm (sol 311–364, $L_s \sim 151°–180°$) are highlighted. (Bottom) MEDA instrument observations including WS measurements over the same period. The WS measurements started on sol 35 ($L_s \sim 22°$) after the commissioning period. The WS was damaged during periods of high convective activity, probably by suspended dust, on sol 313 ($L_s \sim 152°$, WS2) and 315 ($L_s \sim 153°$, WS1).

after ~1500 sols of the mission (Viúdez-Moreiras et al., 2019a, 2019b). As a result of the MY36/2022A RDS, the convective and aeolian activity at Jezero increased dramatically. A close encounter with a dust devil (DD) on sol 313 at 13:42 hr local true solar time (LTST) further damaged WS2 (see the companion paper, Viúdez-Moreiras et al. (2022), hereafter referred to as part 2). Two sols later (sol 315 at 14:24 hr LTST), the damage was produced on WS1 and the MEDA WS was unavailable to provide wind data, leaving only three operative sensor boards: one on WS2 and two on WS1. The sensor was turned off while an engineering analysis was performed. Detailed images obtained with the Mars 2020 cameras (Figure 1) on sol 339 suggested the damage on the board wires due to the impacts of lifted dust. The sensor was again turned on, on sol 342 (L_s ~ 168°), although without retrieving wind data products. Further damage on other boards during the RDS was detected, continuing at sol 413 (L_s ~ 210°) and making the sensor inoperative to retrieve the data without major modifications to the pipeline and additional calibration tests in the wind tunnel. It is expected that wind data from sol 342 to 413, and possibly data since sol 413, will be available when the retrieval algorithm for each boom is modified to focus on the non-damaged boards of the sensor, although greater uncertainty in the wind data will be involved in the retrievals.

2.3. Dust Devil Trajectories as a Background Wind Proxy

In the absence of a working WS, surface winds may be inferred, under particular conditions, from other sensors and/or from their interaction with surface. We have obtained some information on surface winds from DD Navcam surveys or movies after the WS damage. Some surveys or movies detected the passage of DDs, and if conditions were appropriate, it was possible to estimate the trajectory of DDs from cameras. Terrestrial field measurements showed that DD horizontal speed is in agreement with wind speeds a few tens of meters above the surface, and that their horizontal direction closely matches background wind directions (Balme & Greeley, 2006; Stanzel et al., 2008). Despite that Martian DDs could sometimes be much taller than the terrestrial counterparts, it can be assumed at the first instance that DDs move with the background winds near the surface (e.g., Reiss et al., 2014; Stanzel et al., 2008) and therefore the background wind direction can be inferred. Buoyancy-driven turbulent activity present in the PBL during the day can deviate local winds from the background wind, producing continuous disturbances (see part 2); thus, DD trajectories may deviate from the average wind leading to a bias in the inferred wind magnitudes.

Dust lifting events were detected in Navcam surveys or movies. Each comprised 96 × 19° subframed images of 1,280 × 240 pixels. For movies, 21 images were taken over ~90 s at one aim, usually with the camera horizon pointed at some specified azimuth. For surveys, 5 aims were imaged 3 times, with ~4 s between images at one aim. Images were processed following Greeley et al. (2006) by constructing a mean or median frame and subtracting that frame from each image at the same pointing (per-pixel median frames were used for sets of 3). Images were inspected for changing features, all of which were visually confirmed to be lifted dust in motion (excluding obvious illumination artifacts). All reported dust detections were consistent with DDs except one on sol 472 (L_s ~ 248°), which had an amorphous, gust-like appearance. For each set of images with dust lifting, wind direction was assessed visually. Transverse (azimuthal) motion was measured, and radial motion was inferred where possible. Uncertainties range from unconstrained radial motion (45°) to well-constrained radial motion (15°); when multiple DDs were tracked in one sequence, all were used to infer an average wind motion (Stanzel et al., 2008).

2.4. Near-Surface Wind Measurements to Support the Ingenuity Helicopter Flights on Mars

Characterization of the atmospheric environment prior to the first flights of an unmanned aerial vehicle at a particular surface location is necessary to minimize risks during flights. The successful landing of Perseverance on Mars brought with it a partner, the technology demonstration helicopter Ingenuity (Balaram et al., 2021; Farley et al., 2020), designed to demonstrate the capability of powered flight in the Martian environment. Given the absence of a priori atmospheric information in Jezero crater, and the need to understand both density and wind conditions in the local environment, a significant modeling effort was pursued, prior to landing, in order to constrain the expected flight environment (e.g., Mischna et al., 2021). Upon landing, the mission timeline dictated an early demonstration of Ingenuity's capabilities.

Due to engineering constraints on Ingenuity, flights could initially only occur during late morning and afternoon to ensure adequate temperatures for helicopter electronics (dictating the start of the window), and a sufficient battery state of charge to support helicopter heating during the subsequent overnight period (dictating the end of the window). Thus, the Mars 2020 mission focused its first wind observations on a late morning/afternoon period (10 and 17 hr LMST) to support the initial helicopter flights. Preliminary assessment of wind speed and direction was performed, in accordance with the flight constraints, beginning on sol 38 of the mission using calibrated

10.1029/2022JE007522

Table 1

Atmospheric Conditions and Winds During the Ingenuity Helicopter Flights With Available Mars Environmental Dynamics Analyzer (MEDA) Wind Data

F	Earth date (UTC)	L_s (°)	Sol	LTST (hr)	Flight duration (s)	P_{srf} (Pa)	$T_{1.5m}$ (K)	$\rho_{1.5m}$ (kg/m^3)	$\phi_{1.5m}$ (°)	$\sigma_{\phi 1.5m}$ (°)	$v_{1.5m}$ (m/s)	$\sigma_{v1.5m}$ (m/s)	Max $v_{1.5m}$	Min $v_{1.5m}$
01	19 April 2021 07:34	33.5	58.5	12.26	40	748.4	235.8	0.0165	142.1	25.5	5.6	1.8	10.0	1.6
02	22 April 2021 09:33	34.9	61.5	12.29	52	748.6	235.9	0.0165	62.8	56.5	4.0	1.9	9.6	0.2
03	25 April 2021 11:31	36.3	64.5	12.29	80	746.5	236.8	0.0164	85.7	64.1	4.4	1.7	11.2	0.5
04	30 April 2021 14:49	38.7	69.5	12.32	117	748.1	235.3	0.0166	113.9	43.8	4.3	1.7	8.4	0.7
06	23 May 2021 05:20	48.8	91.5	12.45	140	751.7	236.0	0.0166	−39.9	79.2	3.3	1.9	8.9	0.4
07	8 June 2021 15:54	56	107.5	12.54	63	754.8	237.3	0.0166	110.2	39.6	4.6	2.4	12.2	0.3
08	22 June 2021 00:27	61.9	120.5	12.57	77	752.6	238.0	0.0165	78.3	20.0	6.4	2.8	19.1	1.0
12	16 August 2021 12:57	86.1	174.6	13.60	170	715.8	245.2	0.0152	109.6	32.8	3.6	1.3	8.4	0.4
14	24 October 2021 08:18	117.1	241.5	12.92	23	650.7	242.3	0.0140	64.5	31.6	5.7	2.1	11.9	1.0
16	21 November 2021 02:09	130.2	268.5	13.02	108	633.7	240.5	0.0137	42.4	34.0	3.9	1.5	7.9	0.7

Note. Surface pressure (P_{srf}), temperature ($T_{1.5m}$), and estimated density ($\rho_{1.5m}$) at 1.5 m are included as well as mean and standard deviation of wind direction ($\phi_{1.5m}$ and $\sigma_{\phi 1.5m}$) and speed ($v_{1.5m}$ and $\sigma_{v1.5m}$) as measured by MEDA. The direction from which the wind is blowing is shown, $\phi_{1.5m}$, following the standard meteorological convention, where the reference system is $-180° < \phi_{1.5m} \leq 180°$, with the origin pointing to the north. Also, maximum and minimum wind speeds obtained by MEDA during the flights are shown.

MEDA WS data, and showed a favorable environment to fly. First, there was an observed pattern of increasing mean wind speed over the course of the study window, from ∼5 m/s at 10 hr LMST to peak winds of ∼11 m/s by 17 hr LMST (see the companion paper, part 2), in agreement with numerical modeling estimates of large-scale wind speed. The Ingenuity helicopter had previously been tested against mean wind speeds of up to 11.2 m/s prior to launch, with satisfactory performance, and so the MEDA mean wind speed measurements were not considered a significant constraint on the flight window. Second, wind speed variability, or small-scale turbulent activity, decreased modestly throughout the sol, showing a broader range of wind speeds during the late morning and mid-sol period ($\sigma_v < 4$ m/s) with a narrowing range ($\sigma_v \sim 2$ m/s) after ∼15.5 hr LMST (see the companion paper, part 2). This, too, was consistent with modeling studies and reflects the growth of larger-scale convective cells at the expense of small-scale, turbulent motions through the course of the day. The wind direction was not considered a significant constraint on Ingenuity operations, but was monitored for later assessment of helicopter performance.

Based in the large part on this input from the MEDA WS, early Ingenuity flights, starting with the first, historic flight on sol 58, were performed at 12.5 hr LMST, this time being seen as a suitable balance between lower mean wind and a moderate level of turbulent motion, thus minimizing atmospheric risks to helicopter activities. Table 1 shows the atmospheric conditions during the first flights of Ingenuity, for which concurrent MEDA wind data were collected. Figure 4 shows the trajectories for each flight. Mean wind speed during the flights was 4.6 m/s at 1.5 m (7.3 m/s at 10 m assuming a neutrally stable atmosphere, which likely overestimates wind speeds) with a mean pressure and temperature of 725 Pa and 238 K, respectively.

As the team gained confidence in Ingenuity's performance, flights later in the sol were performed as MEDA continued to return data consistent with the previously observed trends. Following each flight, atmospheric data are analyzed to identify any possible environmental conditions that might lead to off-nominal helicopter behavior (though no such conditions have been observed to date). Current challenges for safety at the time of this writing are: (a) in the absence of a working WS (see Section 2.3), seasonal and interannual variations cannot be characterized, nor spatial wind field differences due to topography that the helicopter could experience (see Section 3), and (b) extreme wind speeds detected during wind gust periods and/or during the passage of convective vortices (see part 2) may be highly problematic if the timing and location of these events match the helicopter flight path. Both Ingenuity and future Mars helicopters delivered as part of the Mars Sample Return project will have to deal with this trouble.

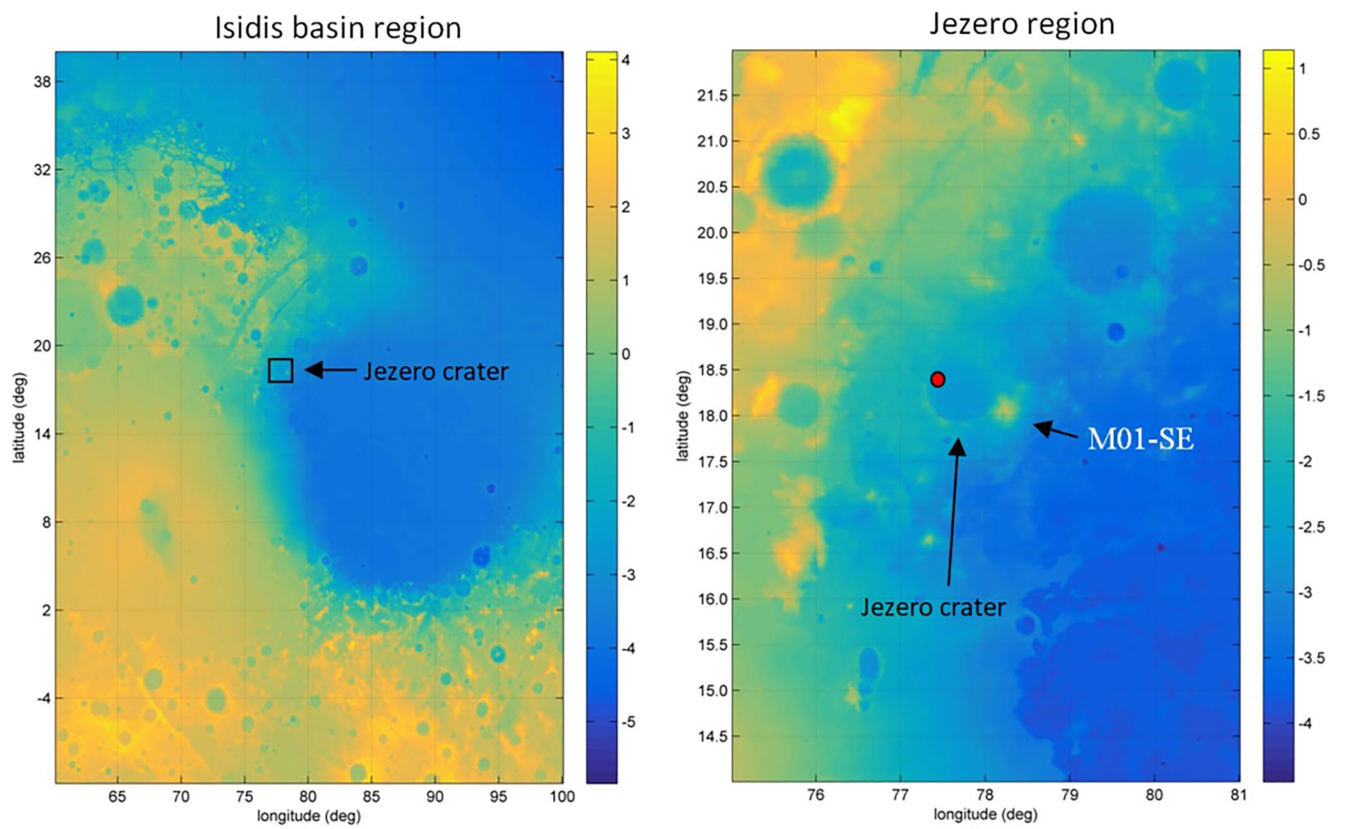

Figure 3. (Left) Mars Orbiter Laser Altimeter topography for the Isidis basin region. (Right) Enlargement for the Jezero crater region. Perseverance's location is highlighted with a red circle close to the northwest crater rim of Jezero crater. Altitude is shown in kilometers both in left and in right panels. The mountain located close to the southeastern crater rim of Jezero is highlighted in the right panel (hereafter referred as M01-SE, see text).

3. Influences in the Jezero Crater Circulation

Surface wind patterns in the tropical region of Mars could be the consequence of complex interactions between slope flows, on regional and local scales, and the large-scale circulation, dominated by Hadley cell flows, thermal tides, and other planetary waves. In addition, other topographic influences, microscale flows, turbulence, and wave activity modify this situation.

Jezero is an impact crater of 45 km in diameter and more than 500 m deep from its surroundings with crater rims elevated ∼800 m to the W and ∼1 km to the S above the crater floor (e.g., Schon et al., 2012). Jezero is located on the northwestern slopes of Isidis basin (Figure 3), a region presenting a steep slope (∼0.7° downward toward ∼120° of azimuth, clockwise from the north). This slope suggests strong near-surface regional flows in the area. In fact, the Isidis regional slope in the Jezero region is significantly greater than the <0.1° general slope of other landing sites, for example, for VL 1 and InSight, where wind patterns were significantly shaped by regional slope flows (e.g., Banfield et al., 2020; Hess et al., 1977; Viúdez-Moreiras, Newman, et al., 2020). Thus, it was expected pre-landing that the regional flows on the Isidis basin slopes may shape the surface wind patterns.

Additionally, local dynamics were expected in Jezero crater. To date, the only mission to measure winds in a region with significant topography at the local scale was MSL, which operates inside Gale crater. MSL observed wind patterns shaped by local slope flows related to both the rim of the crater and the mountain in the center of Gale (Newman et al., 2017; Viúdez-Moreiras et al., 2019a). Perseverance's landing site is close to the western-northwestern rims of Jezero crater, where slope flows are expected to develop. However, Jezero crater is smaller and far shallower than Gale crater and does not contain a central mound, so the potential relevance of local slopes on wind patterns should be addressed by observations and modeling.

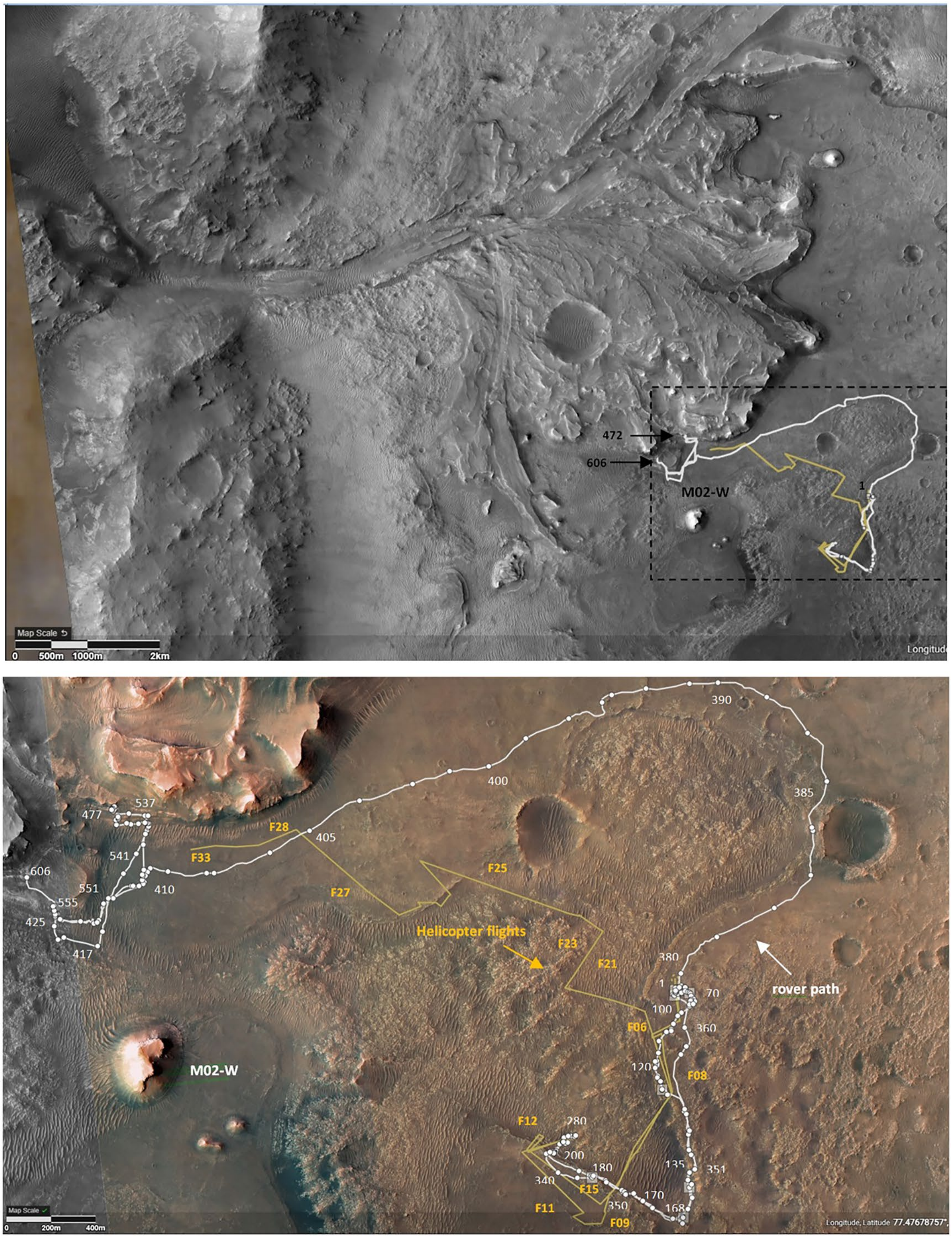

Figure 4. High-resolution images of the landing site location close to the western crater rim, taken from Mars Reconnaissance Orbiter. (Top) Crater rim and Jezero's delta, covering ~18.40°–18.56°N of latitude and ~77.24°–77.47°E of longitude. (bottom) Enlargement of the southeastern region around the Mars 2020 landing site. The Perseverance rover and the Ingenuity helicopter trajectories as far as sol 606 ($L_s \sim 330°$) are highlighted in the bottom panel in white and yellow colors, respectively. Mission sols are included in black, and helicopter flights are labeled in yellow. The mountain located to the west is highlighted in both panels (hereafter referred as M02-W, see text).

Another influence in the observed wind patterns by a mobile platform is the change in location throughout its traverse, that is, surface winds are observed in this case by a rover instead of by a fixed platform. It enables its wind data to also shed light on changes to wind patterns with location, although there is difficulty differentiating these variations with seasonal variations if the same location has not been sampled multiple times. There is a precedent on Mars. The Curiosity rover traveled many kilometers from the bottom of the northwest region of Gale crater toward Aeolis Mons, a feature of more than 5 km altitude at the center of the crater. Along its traverse, the rover characterized the Bagnold Dune field around local winter in the third Martian year of operations (Newman et al., 2017) and measured upslope winds during the daytime getting stronger as it climbed Aeolis Mons (Viúdez-Moreiras et al., 2019a, 2019b).

After exploring the delta remnant inside the crater, Perseverance will drive to the rim and out of Jezero, likely driving to explore regions to the southwest. Different local dynamics are expected both closer to the rim, where local downslope flows at night are expected to be much stronger, and outside the crater. Prevailing easterly–southeasterly winds are inferred from satellite images though analysis of the aeolian features (Figure 4, bottom; Day & Dorn, 2019). In addition, channeling effects and flow deviations closer to the crater rim and delta walls can be observed in those images (Figure 4, bottom). This is particularly easy to observe close to topographical features such as to the left of the mountain located to the west (hereafter M02-W, Figure 4, bottom). Focusing on Perseverance's trajectory, significant deviations from the prevailing winds can be expected at least between sol 380 and 385 (where aeolian indicators suggest dominant east-northeasterly winds instead of the prevailing east-southeasterly winds) and between sol 400 and 408 (where aeolian indicators suggest channeling effects by small-scale topography, and dominant northeasterly winds, Figure 4, bottom). After sol 410 ($L_s \sim 208°$), the rover is very close to the delta walls (Figure 4, top), which may also imply disturbances in the observed winds. However, during the first 315 sols of the mission, that is, the timescale currently covered by the WS, the rover moved within a region of only ∼1 km^2 (Figure 4, bottom), in which strong variability neither in topography nor atmospheric dynamics is expected. Therefore, we initially assume that the observed variability in the MEDA wind data is due to the different temporal scales and dust events.

4. Diurnal Variation of Surface Winds at Jezero

4.1. Observed Diurnal Wind Patterns

The Perseverance rover measured surface winds at Jezero during the first 315 sols of the mission with observations starting at sol 35 (Section 2). This corresponds to areocentric solar longitudes (L_s) from ∼22° to ∼153°, that is, much of northern spring and summer.

The observed wind patterns at Jezero presented minor sol-to-sol variations that were generally overwhelmed by the diurnal variations in accordance with observations from previous missions on Mars outside the dust storm season (e.g., Banfield et al., 2020; Hess et al., 1977). The acquisition strategy involved in Mars 2020 operations (Section 2) prevented complete measurement of the diurnal cycle in a single sol; therefore, multiple sols were necessary to fill the gaps, which were particularly of concern during the afternoon due to more gaps at that time (Figure 2). No major variability was observed in the general shape of the diurnal cycle within the period of observation. Conversely, a mostly repeatable diurnal cycle was measured with minor long-term variability (detailed in the next subsection).

The observed diurnal cycle of winds presented two regimes: (a) a daytime or convective regime, from dawn to sunset, with average easterly to southeasterly winds in which maximum wind speeds were measured, and (b) a nighttime regime with a period of W-NW winds followed by a relatively calm period until sunrise with highly variable wind directions as a function of sol and time of night. In addition, two transition periods occurred between the daytime and nighttime regimes. Figure 5 shows the diurnal variation in wind speed and direction, averaged in 10-min windows over a period of 40 sols close to the northern summer solstice, which is illustrative of the observed diurnal cycle throughout the first 315 sols of the mission.

Over this sol period, winds were southeasterlies during the morning when the PBL was developing. They gradually rotated east as the day progressed, at the same time that wind speed strongly increased. Maximum 10-min-average wind speeds of ∼7 ms^{-1} were measured during the late afternoon (∼17 hr LTST), when winds were easterlies. This corresponds to the time of sol when the solar heating that drives daytime upslope winds had lasted for several hours but was declining and would shortly be very low at sunset (∼18.5 hr LTST). In addition, the wind variability, both in wind speed and direction, was strongly reduced in the afternoon, when the PBL was fully developed and when turbulence was likely dominated by larger eddies. Winds remained as east-northeasterlies in the afternoon, while wind speed decreased abruptly at 17.5 hr. After sunset, wind speeds continued decreasing,

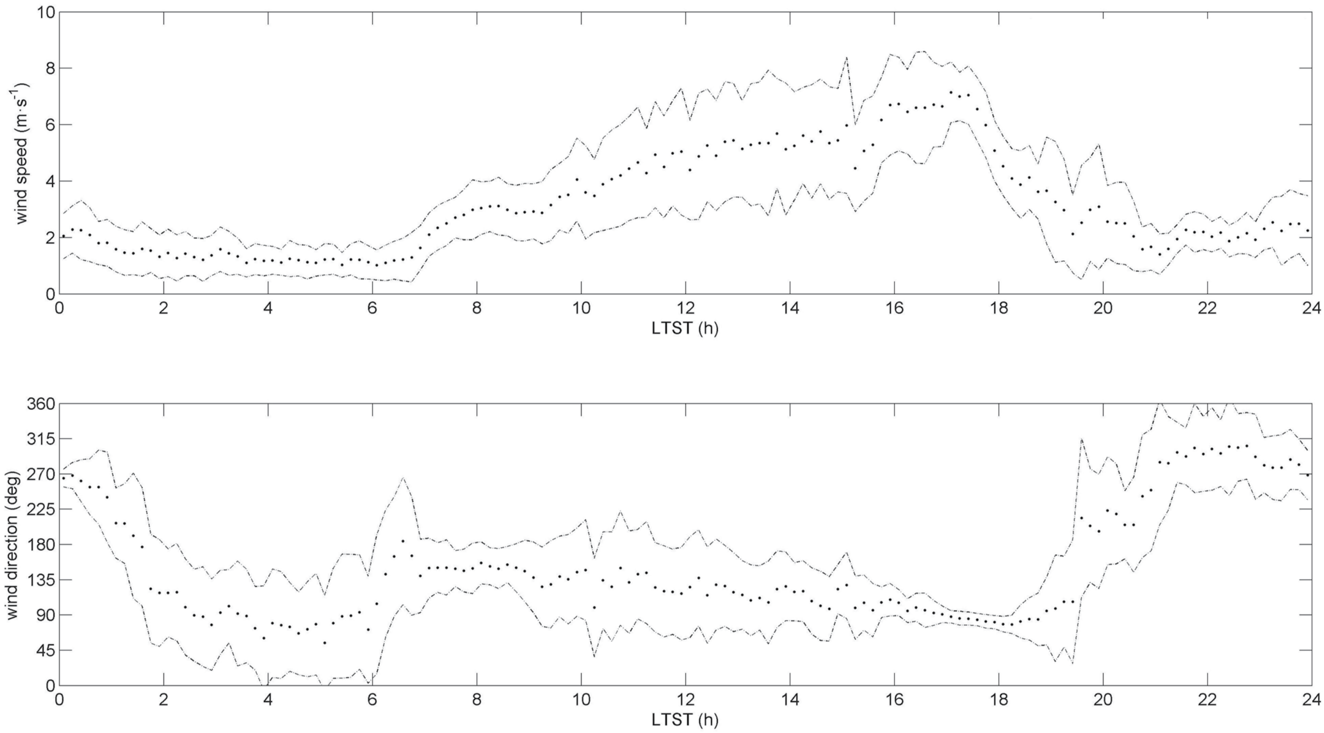

Figure 5. Diurnal variation in wind speed and direction as a function of local true solar time (LTST) over a period of 40 sols close to the northern summer solstice ($L_s \sim 90°–120°$). The direction from which the wind is blowing is shown, following the standard meteorological convention. 10 min averages are shown as dotted lines with the ± one standard deviation shown in dashed lines.

while winds inverted the rotation that presented throughout the daytime, rotating clockwise by a few degrees from east-northeasterlies to east-southeasterlies from 18.5 to 19.5 hr. At 19.5 hr, the daytime convective regime had ceased, and wind speeds were weak at 2–3 ms^{-1}. The winds then dramatically rotated clockwise from easterlies to west-northwesterlies between 19.5 and 21.5 hr. This rotation was coincident with a wind speed spike in some sols that lasted for roughly an hour; others presented a local minimum in the diurnal cycle of wind speed. Wind directions were then stable for ∼2 hr with a slight shift toward westerlies. After ∼21.5 hr, wind speeds gradually increased, peaking with a local maximum around midnight. A subsequent decrease produced the minimum wind speeds reached during the diurnal cycle, ∼1 ms^{-1}, in a period characterized by a counterclockwise rotation toward easterlies and with pronounced variability in wind direction compared to that observed during the day. This period was characterized as well by a strong sol-to-sol variability (see Section 5). Finally, half an hour after dawn (∼5.5 hr LTST), winds rotated clockwise to S-SE and increased in intensity as the PBL developed, completing the diurnal cycle.

Notably, the observed variability represented in Figure 5 by the standard deviation of wind speed and direction as a function of LTST described above could, a priori, be due to both intrasol (sub-diurnal) and intersol variations, given that 40 sols were averaged in this figure. Further analysis of such variability shows that, in general, intrasol variability dominates during the daytime convective regime (turbulence scale), while intersol variability dominates the ensembled multi-sol pattern during the night regime (see part 2).

4.2. Mechanisms Affecting the Diurnal Cycle in the Near-Surface Wind Patterns

The timing and magnitude of the observed regimes are consistent with control by slope flows. During the daytime, mean wind direction matched the regional upslope of Isidis basin at Jezero region and the Jezero crater rim slope (Figure 4), although the wind direction shifted by ∼30° north once the upslope winds were fully developed in the late afternoon. This could be explained by upslope flows being perturbed by the topography at Jezero region together with the effect of local upslope flows. A full rotation of winds was produced after sunset, when near-surface vertical thermal gradients started to reverse after their daytime maxima due to surface cooling.

Winds presented after rotation roughly an opposite direction, that is, at that time, the wind direction roughly matched the downslope of Isidis basin around the Jezero region and the crater rim slope. This strong control by regional and/or local winds is predicted by pre-landing GCMs and mesoscale simulations (Newman et al., 2021; Pla-García et al., 2020). The modeled winds usually ranged from northeasterlies to south-southeasterlies during the daytime, rotating to westerlies/northwesterlies after sunset. The fact that the direction of the slopes of Isidis basin and Jezero crater's western rim is similar makes discerning the mechanism that modulates the diurnal cycle at the landing site difficult. Newman et al. (2021) suggested that largely similar wind patterns between the high- and low-resolution simulations tested in the study during the daytime could indicate that the slopes of Jezero crater, itself, cannot drive the winds during the daytime as the local scale is not resolved in the latter simulations. In any case, the low-resolution simulations may be shifting the daytime wind direction by some degree, due to the variability in the Isidis basin slope direction at Jezero region (Figure 3), thus artificially mimicking the potential effect local anabatic winds have on the wind pattern. On the other hand, given the small size of Jezero crater (less than 50 km), it is expected that upslope flows on the eastern crater rim and on the mountain located close to the southeastern crater rim of Jezero (hereafter M01-SE, see Figure 3) would act in opposition to the regional flow, consequently producing effects at the landing site location. In that case, local forcing would produce complex constructive and destructive interactions in the near-surface winds.

The gradual increase in wind speeds and the shift in wind direction as the daytime timeslot progressed can be interpreted as the result of the gradual and different increase in the relative strength of regional and local slope flows as the PBL develops as reproduced in the model simulations to some extent. Therefore, regional and local upslope flows would dominate during the daytime. Also, the relevance of regionally induced flows by thermal tides, hereafter referred to as tidal flows, cannot be ruled out during the daytime. However, the complex structure of tidal flows and the weak diurnal and semidiurnal tides at Jezero, together with their representation in models being sensitive to the three-dimensional dust distribution used, complicates discerning the relative contribution of tidal flows under nominal conditions.

The vertical extent of the slope winds and the gradual coupling with winds aloft should also be considered. The unstable daytime PBL present in the Martian atmosphere quickly transports momentum between the near-surface and the atmosphere several kilometers above. Hess et al. (1977) attributed the behavior observed by VL1 to a combination of near-surface slope flows, peaking in the mid-afternoon, and maximum turbulent coupling with the winds aloft, peaking in late afternoon and acting constructively with the former. In addition, the analysis of the wind data acquired by the InSight Lander at Elysium Planitia suggest that the reduction, or perhaps entire lack, of significant coupling during the nighttime could have allowed downslope flows to develop, producing surface winds opposite to the strong winds from the general circulation present during the northern summer in Elysium Planitia.

We performed MarsWRF GCM simulations in order to test the possible coupling of large-scale winds into near-surface winds in the Jezero region with the same version and setup successfully applied to previous studies for the Gale crater region (Richardson & Newman, 2018; Newman et al., 2017; Viúdez-Moreiras, 2021; Viúdez-Moreiras et al., 2021), but using here only the global domain. We focused on the evaluation of the interference between the large-scale and the regional slope winds on the northwestern slopes of Isidis basin, so it is not necessary to resolve the local circulation at Jezero crater. These simulations show that surface winds on the slopes of the Isidis basin are mostly insensitive to the higher winds in and above the PBL due to the strength of daytime slope flows on Isidis's slopes.

The effect of mid-latitude westerly winds above the PBL can be observed outside summer (Figure 6), indicated by the strong westerly circumpolar winds that reach the Isidis basin latitudes, and that are variably disturbed by tidal flows along the day. Within the jet streams, these winds can present velocities greater than 100 ms^{-1} at high altitudes (Mitchell et al., 2015) and reach lower latitudes nearer the surface with reduced wind speeds. Simulations presented in Figure 6 show that the daytime PBL at Jezero's region is subjected around the equinoxes to midlatitude westerly winds that oppose the regional upslope near-surface flows. These strong winds are slightly disturbed by tidal flows along the day. Conversely, around the northern summer solstice, these westerly winds are not present and winds above the PBL are dominated by tidal flows, which act constructively to the near-surface winds during most of the daytime, particularly during morning and midday. The vertical extent of the surface regional upslope winds produces even strong winds at a couple of kilometers above the surface during the daytime (Figure 6b). At Jezero's region, the PBL reaches in the afternoon ~8 km at northern summer and

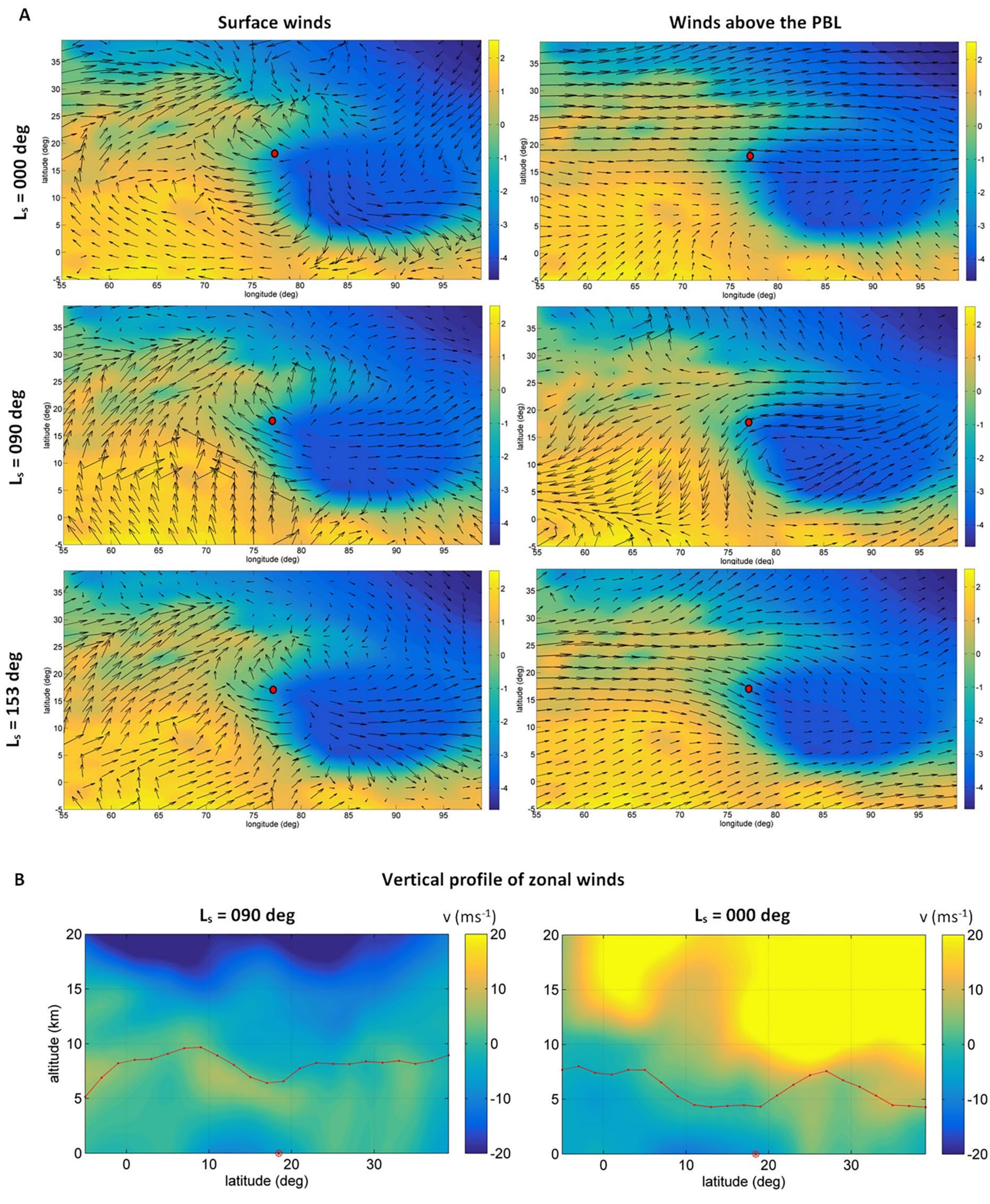

Figure 6. (a) Wind field at midday in the Isidis basin region from MarsWRF General Circulation Model simulations at northern spring equinox (top), summer solstice (middle), and at $L_s = 153°$ (bottom), averaging ±5 sols. Surface winds and winds above the planetary boundary layer (PBL) (10 km) are shown in the left and in the right columns, respectively (see text). Topography is shown as color-coded elevation (km) from the Mars Orbiter Laser Altimeter, both in left and in right panels. Wind fields are shown at noon time at the center of the domain. (b) Midday vertical profile of zonal winds at the landing site's longitude. Pseudo-altitude in km. The PBL depth at landing site's longitude is represented by a red line as a function of longitude. The wind speed axis is constrained to ±20 ms^{-1} to better observe the range in Isidis basin. Jezero crater is shown by a red dot.

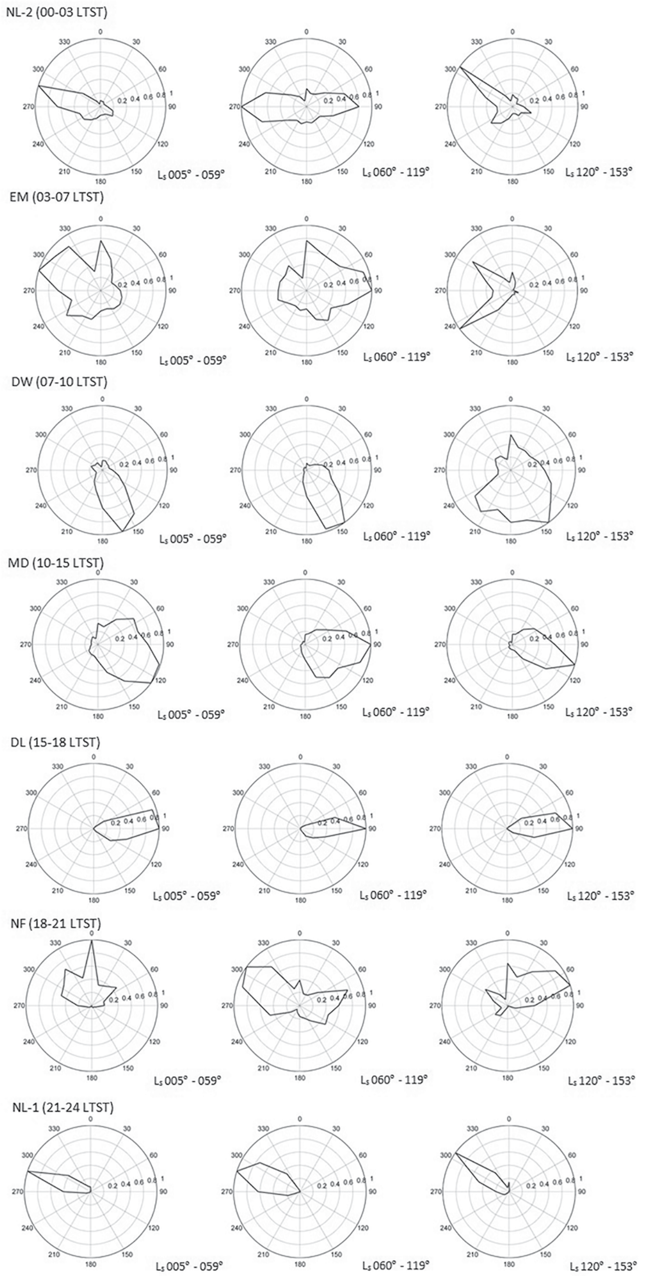

Figure 7. Wind roses as a function of areocentric solar longitude (L_s) and time of the day until the wind sensor failure on sol 315 (L_s ~ 153°). Results are shown for three seasonal periods (L_s 5°–59°, 60°–119°, and 120°–153°) and seven diurnal timeslots covering the diurnal cycle (see text). The radial axis shows the probability for each wind direction. The direction from which the wind is blowing is shown, following the standard meteorological convention.

~5 km close to the equinoxes, achieving greater values at the fall equinox than at the spring equinox. However, although the winds above the PBL can strongly affect the high layers within the Isidis basin's PBL (Figure 6b), simulations suggest that the effect on the surface winds by the winds above the PBL is minor, even when winds above the PBL flow in opposite directions to the surface winds (Figure 6a), due to the intense daytime regional slope flows, present in the Isidis basin's slopes. The intense regional slope flows would also contribute to suppress the daytime PBL regarding the Jezero surroundings. Most of the slight differences observed in the near-surface patterns on the Isidis basin western slopes could be attributed to the variation in the Hadley cell circulation from a weakly dual-Hadley cell equinoctial circulation to a stronger single cell present around the summer solstice producing zonal-mean near-surface southerly winds. These results are in agreement with the weak southerly shift in surface winds observed in several model pre-landing predictions for Jezero around southern summer (Newman et al., 2021), which may be attributed to the Hadley cell circulation, although other models do not present such a shift. It illustrates how the steep slopes of Isidis basin would be contributing to isolation of the circulation from the large-scale dynamics in the Jezero region.

The nighttime regime presents several interesting features with some differences from the daytime scenario. An interesting feature is the effect of the nighttime PBL structure on the near-surface winds. While the daytime PBL quickly transports and mixes momentum between surface and several kilometers of height, the nighttime PBL is much shallower, maximizing the effect of small topographic features in their surroundings that may reinforce mechanical turbulence in these areas and affect the downslope wind intensity and direction. The Jezero region and Jezero crater itself contain significant topography (Figure 2) that could dramatically affect the nighttime patterns in the mesoscale (hundreds of kilometers to 1 km) and in the microscale (1 km to hundreds of meters). The first part of the night, from sunset to 01 hr LTST, was characterized by relatively stable westerly/northwesterly winds that peaked around midnight as a likely result of downslope winds peaking at that time. However, this is not what is expected from regional downslope flows, which should peak right before sunrise, as the thermal conditions that drive katabatic flows (i.e., surface cooling along slopes) grow overnight. Pre-landing atmospheric modeling from lower-resolution simulations (i.e., that did not resolve the topography of Jezero crater) predicted that regional slope flows at the Perseverance landing site would, in general, grow during most of the night, reaching peak values shortly before sunrise (Newman et al., 2021), which is not at all what is observed. Atmospheric modeling from higher-resolution simulations (i.e., that did resolve the crater topography) predicted a spread of results with the MarsWRF modeling reproducing the observed peak around the midnight followed by a drop in wind speed to low values by 02–03 hr. MarsWRF also shows that winds aligned with the Isidis basin downslope direction are, on average, present across this general region at night, but are absent from the center of Jezero crater, with the strongest winds (both in the crater and outside) instead linked to smaller-scale topography, including strong downslope winds around the western crater rim. This supports the hypothesis that regional downslope winds are weakened by the Jezero topography and that local downslope winds on the western crater rim dominate during this timeslot (e.g., Newman et al., 2022).

After 01 hr LTST, winds decreased in intensity and rotated counterclockwise to variable directions, although easterly winds dominate, with dramatic variability over most of the night (Figures 5 and 7). This reduction in the relative strength of the crater rim downslope winds was probably enhancing the effect of another mechanism that was competing with the previous one. An analysis of the topography around the landing site and the prevailing wind directions in this period indicates that the best candidates to provoke such easterly flows should be the downslope winds at the eastern crater rim, possibly reinforced by downslope flows on M01-SE. Such flows would compete with the western and other crater rim flows, provoking convergent flows on the crater floor and periods of high mechanical turbulence and wind variability. The nocturnal dynamics may also increase the likelihood of low-level jets at the nocturnal inversion interface perhaps affecting the Perseverance's landing site in particular times (Pla-García et al., 2022). The very low wind speeds observed during this period of the night suggest that these convergent flows are very weak or a destructive interaction around the landing site dominates the atmospheric dynamics, provoking a calm region on the crater floor, at least at the Perseverance landing site. The calm period observed in Jezero crater at night resembles what was observed in the early morning at Gale crater, where the available data showed very low wind speeds (Viúdez-Moreiras et al., 2019a, 2019b) probably driven by a similar mechanism (in that case due to downslope flows in Aeolis Mons and the northern crater rims, greatly isolated from the regional and large-scale circulation).

5. Sol-to-Sol and Seasonal Variability in Winds

5.1. Potential Mechanisms Affecting the Seasonal Cycle in the Near-Surface Wind Patterns at Jezero

The general circulation at the time of Perseverance's landing ($L_s \sim 5°$) is characterized by a weak equinoctial Hadley cell circulation, when the return branch of the northern cell would produce zonal-mean near-surface northerly winds at Jezero's latitude. Thermal tides and planetary waves are also affecting the large-scale circulation. In addition, strong westerly circumpolar winds aloft in the area reaching the PBL can be observed in the simulations (Section 4.2 and Figure 6).

The situation changes as the season progresses. Together with possible changes in the intensity of regional and local slope flows, and seasonal variations in tides and planetary waves, the dual cell becomes a single cell that is already developed by summer solstice (L_s 90°) with upwelling (downwelling) at northern (southern) midlatitudes, producing near-surface southerly winds in the zonal mean. The effect of the Hadley cell on surface winds is to a greater or lesser extent evident in the surface wind data of past missions. Viking 1 data suggested a transition from regional topographic to global Hadley circulation control of the winds above the landing site with a remarkable effect on the surface winds measured by the lander (Murphy et al., 1990). The MSL wind data confirmed model simulations that predicted the large-scale, synoptic (>100s of km in scale) flow has a much stronger influence at Gale Crater during the summer and winter seasons when a single Hadley cell exists in the zonal mean (Newman et al., 2017; Rafkin et al., 2016; Viúdez-Moreiras et al., 2019a). InSight data at Elysium Planitia indicated that the observed wind patterns resulted from the interaction between regional and local slope flows induced by topography, which all produced a diurnal perturbation superimposed on a mean flow, dominated by a combined effect of the Hadley cell and channeling effects from the regional topography (Banfield et al., 2020; Viúdez-Moreiras, Newman, et al., 2020). However, although evident, the effect of meridional circulation in Mars 2020 wind data is difficult to observe due to the dominance of regional and local slope flows and the lack of measurements in northern winter, the season when the mean meridional circulation is at its strongest (e.g., Richardson & Wilson, 2002). Also, it is possible that the topography and variability in the terrain properties of this region could be influencing the behavior of the meridional circulation from the zonal mean.

5.2. Observed Sol-to-Sol and Seasonal Variability in Daytime Winds

Figure 7 presents the wind roses for three L_s ranges and seven periods of the day or diurnal timeslots. The latter are chosen to combine hours with similar wind patterns, taking into account that the inherent complexity of the surface wind patterns may imply variations within the diurnal timeslot, as we will describe in that case. We use the same timeslots and nomenclature as presented in Viúdez-Moreiras et al. (2019a, 2019b) for Gale crater. Local times are hereinafter referred to, except in cases where another timeframe is explicitly indicated, as LTST. The diurnal timeslots are: (a) morning (DW), from 07:00 to 10:00, (b) midday (MD), from 10:00 to 15:00, (c) afternoon (DL), from 15:00 to 18:00, (d) night-fall (NF), from 18:00 to 21:00, (e) night (NL-1), from 21:00 to 24:00, (f) midnight (NL-2), from 00:00 to 03:00, and (g) early morning (EM), from 03:00 to 07:00. The time evolution of wind speed and direction is presented in Figure 8 for selected diurnal timeslots, similar to those used

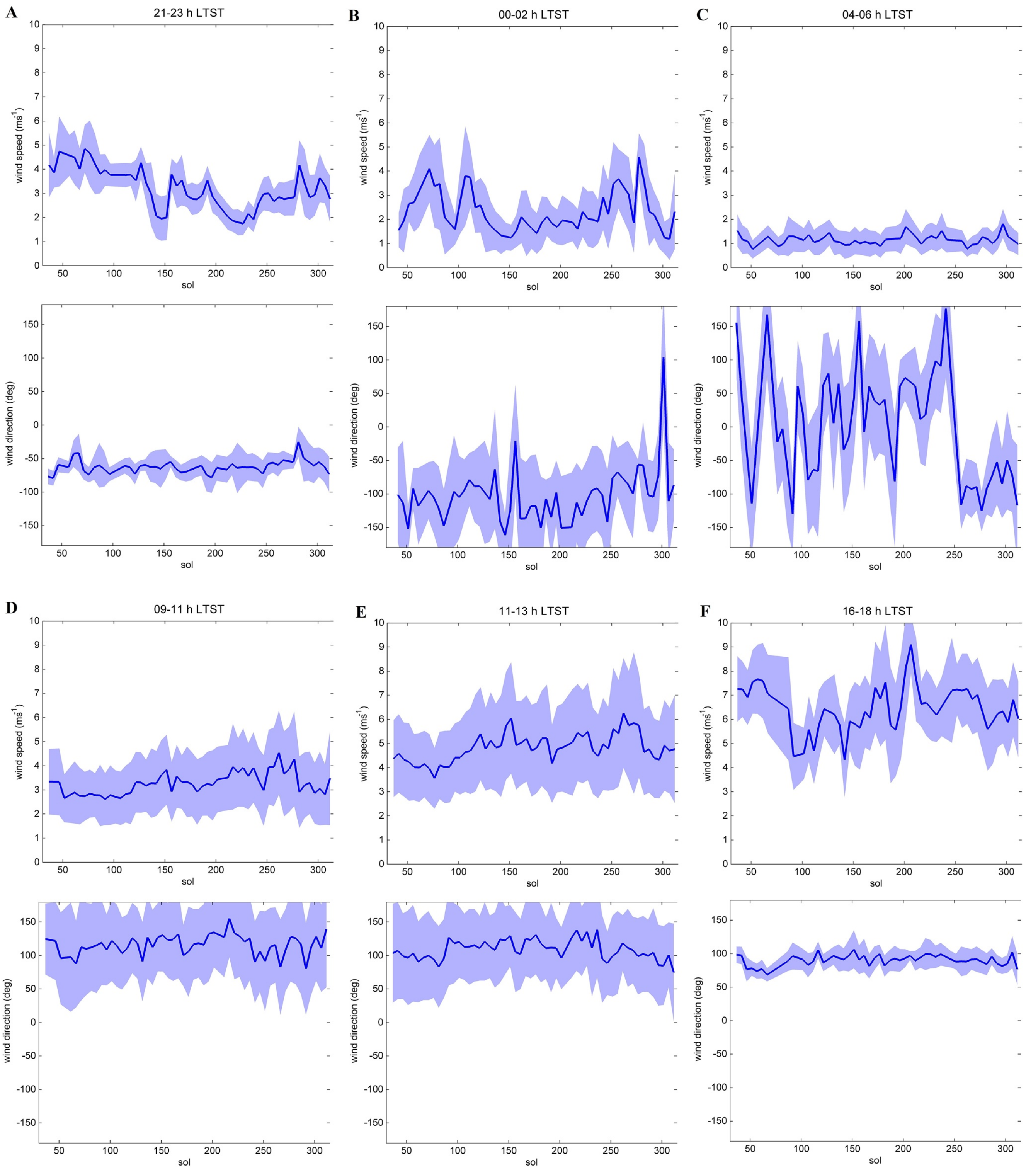

Figure 8. Evolution in 5-sol average wind speeds and directions as a function of sol for different diurnal timeslots (a–f) during the nighttime and daytime with the ± one standard deviation shown by the light blue shading.

in Figure 7 but with slight modifications to allow for a better representation of the data as a function of season given short-term data gaps present in certain periods.

One-sol averages give more information about different dynamic processes that affect particular periods of time, but the significant gaps involved in the wind data (particularly between 16–17 and 16–18 hr in the early sols of the mission) make it difficult to study the sol-to-sol variability systematically. Therefore, 5-sol average wind speeds and directions as a function of sol are presented in Figure 8.

Overall, the seasonal variability for the winds observed by Mars 2020 between the northern spring and the summer season was weak (Figure 7), without dramatic variations, in agreement with the dominance of the regional and local scales in the surface wind patterns (Section 3).

During midday (MD diurnal timeslot in Figure 7), when upslope winds were developing, prevailing southeasterly winds were measured during early spring. Significant sub-hourly variability was observed mainly due to turbulent scales (see part 2), which included measuring northeasterly and south-southeasterly winds at certain times. These variations overwhelmed intrasol and seasonal variations (Figure 8). Over the summer solstice, prevailing winds turned to east and east-southeasterlies. The seasonal variation of wind speeds peaked at that season (see part 2). During the afternoon (DL diurnal timeslot in Figure 7), the full development of regional slope flows overwhelmed the effect of other potential mechanisms in the large scale, maintaining roughly constant behavior in wind directions as a function of season. The low variability in the wind direction that characterized this timeslot, probably due to the reduction in short-term eddies as the PBL was fully developed (Section 4), was maintained as a function of season.

The nightfall (NF) diurnal timeslot in Figure 7 (18:00–21:00) is a period of transition between anabatic upslope winds and katabatic downslope winds and shows strong sensitivity to season. Counterclockwise rotation started in the first sols of the mission at ∼18 hr (sunset at ∼18.25 hr) with northerly winds at 19.5 hr and north-northwesterly winds at 22.5 hr as a result of local downslope winds dominating at that time. As the mission progressed, the transition began later and occurred more rapidly. Right before the summer solstice, the rotation was suddenly executed at 19–19.5 hr (sunset at ∼18.5 hr). Right after the solstice, the sign reversed, that is, the rotation was performed clockwise and the transition was very slow (Figure 5). At mid-summer, the transition reversed again to counterclockwise rotation but with longer timescales typically observed in the first sols of the mission and beginning a bit later. This seasonal behavior in the transition between upslope and downslope winds could be related to a coupled effect of Hadley cell return flow and thermal tides. In fact, more southerly winds are expected as approaching toward solstice, which is consistent with the change to a clockwise rotation. However, the different behavior between pre-solstice and post-solstice would need the effect of another mechanism acting together. As described, thermal tides produce variable tidal forcing as a function of time of day and as a function of season. We observe significant changes in the phase of the diurnal pressure mode and also a peak in the amplitude of the semidiurnal pressure mode after the summer solstice (e.g., Sánchez-Lavega et al., 2022). These changes suggest disturbances in tidal flows at that season, which could relate with the different behavior in the rotation at that period.

5.3. Sol-to-Sol and Seasonal Variability in Nighttime Winds

West-northwesterly downslope winds were fully developed in the first part of the NL-1 timeslot in Figure 7 (21–24 hr), which remained roughly constant throughout the mission and presented very little variability in wind direction, similarly to that produced with the counterpart daytime upslope winds during the afternoon. However, the longer rotation duration at mid-summer from the daytime winds coincided with a slight shift in the wind directions to northwesterly winds; that is, the local downslope winds had a greater northerly component as the summer progressed. The intensity of midnight wind speeds, affecting the NL-1 and NL-2 timeslots, reduced to one half of the 4–5 ms^{-1} observed at the beginning of the mission. Stable atmospheric conditions during the night likely promoted the effect of topography on surface flows; and significant topographic features in the surroundings such as the delta walls and crater rims, but also M02-W (Figure 4), could result in spatial differences in nighttime flow among rover locations as the mission progressed. In fact, extreme shifts in wind direction can be inferred from aeolian signatures in the MRO images close to the delta and in other topographical features (Figure 4) with the delta walls producing what appears to be a channel effect in the surface flows on the area (Section 3).

However, the observed variability as the mission progressed is mostly attributed to seasonal variations (Section 3). It would include the effect of the large-scale circulation on the regional and local scales during nighttime. Convergent local downslope flows on the crater floor during NL-1 and part of NL-2 were probably competing, in the context of prevailing regional downslope flows from the west-northwest, and with local downslope flows from the east-southeast likely reinforced by M01-SE. A single cross-equatorial Hadley cell that develops around summer solstice would produce zonal-mean southerly winds near the surface; these could compete with the slope flows, reducing the intensity of the regional downslope flows in this region (northwesterly flows), in addition to local slope flows with such meridional and zonal wind components, hence enhancing the effect of east-southeasterly local downslope winds. This situation would reduce the strength of the northwesterly winds around midnight, as described earlier, and it was likely the responsible for the winds from the east-southeast observed at the Mars 2020 landing site around the summer solstice (Figure 7, EM timeslot).

The second part of the night (NL-2 diurnal timeslot in Figure 7, 00–03 hr) contains another transition in which the intensity of the downslope winds in the crater rim decreased, starting a calm period extending as late as the sunrise (Section 4). The NL-2 and EM diurnal timeslots in Figure 7 involved the greatest wind variability observed in the diurnal cycle, both in wind direction and in the relative wind speed variability (see part 2). During the first sols of the mission, the local downslope flows reduced their activity well enough to produce a counterclockwise rotation toward easterlies at the end of NL-2. Weak easterly winds developed in some sols at the end of this timeslot, while other sols had variable winds during the calm period. Around summer solstice, the reduction in the intensity of downslope flows and the subsequent rotation to easterly winds were more established, taking place in the middle/end of NL-2. After L_s 120°, the situation was the reverse of that observed in the first sols of the mission. Some sols maintained the downslope flows more often than others. This curious effect can be seen in Figure 8 (00–02 hr). The dramatic increases between sol 60–80 (L_s ~ 34°–43°) and between sols 110–120 (L_s ~ 57°–61°), as well as some periods between sols 250 and 280 (L_s ~ 121°–135°) are the result of variable downslope flows that have an influence longer into the calm period during the night and early morning (NL-2 and EM timeslots) and can be related to the lack of a competing mechanism such as the Hadley cell circulation, which is present around the summer solstice.

The EM timeslot (03–07 hr) in Figure 7 involved the greatest variability due to a combined effect of intersol and intrasol variations. After L_s 120°, westerly winds developed again around 5 hr, but with much less intensity than those observed at midnight, before the development of upslope winds in the morning (see the DW, 07:00–10:00, timeslot in Figure 7). As described above and in Section 4, these rich nocturnal dynamics could result from downslope flows at the eastern crater rim, possibly reinforced by downslope flows on M01-SE. Such flows, likely promoted around southern summer by the Hadley cell, would compete with the western and other crater rim flows, provoking destructive interaction by convergent flows on the crater floor, and periods with high mechanical turbulence, and hence, wind variability. The dramatic seasonal rotation observed during this timeslot (Figure 7) suggests large-scale interference in the Jezero region circulation.

5.4. Atmospheric Waves as a Source of Sol-to-Sol Wind Variability

Most of the intersol variability is the result of stochastic variations produced by turbulence and interactions with the different scales. However, part of the observed intersol variability in winds can be associated with atmospheric traveling waves, possibly baroclinic. The effects of baroclinic waves were clearly observed in the VL wind data, particularly by VL-2, which landed at 48°N, but also in VL-1, which landed at 22.5°N (e.g., Barnes, 1980, 1984). These disturbances have also been observed in the InSight wind data (Banfield et al., 2020), which landed in equatorial latitudes. Mars 2020 has detected traveling waves in the pressure and temperature data (Battalio, 2021; Sánchez-Lavega et al., 2022) with variable periods during the mission. MEDA wind data are constrained between L_s ~ 22° and ~153° and have many gaps (Section 2) particularly in the first sols of the mission, which challenge the detection of traveling waves. After detailed analysis of the wind data, we are reporting the effects of traveling waves on the surface winds at Jezero.

There are several sol periods with a predominant period of oscillation; they are mostly weak and uncorrelated with pressure. However, a strong peak appears in the frequency analysis between sols 130 and 170 both for wind and pressure variables, corresponding to waves of 4.4-sol period with ~0.6 ms^{-1} amplitude both in wind speed and pressure. Figure 9 shows the wind- and pressure-detrended signals (top and bottom, respectively) around sol 150 (L_s ~ 75°, closer to the northern summer solstice). This sol period is characterized by a clear harmonic in the

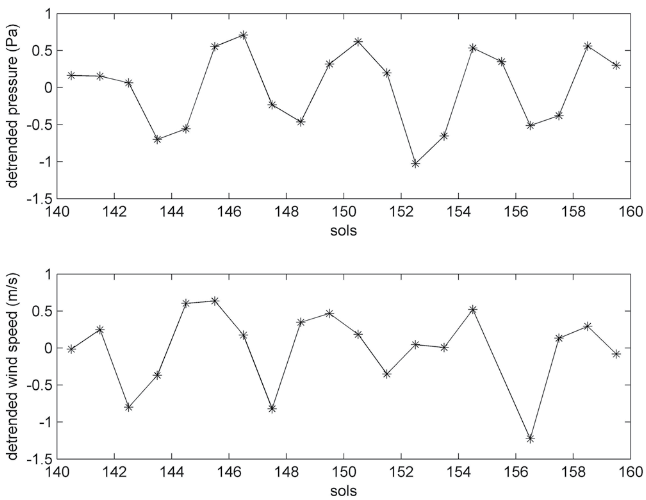

Figure 9. Detection of oscillations probably related to traveling waves in the Mars 2020 wind data. Detrended pressure (top) and wind (bottom) signals are shown around sol 150 (L_s ~ 75°, closer to the northern summer solstice), after removing the subdiurnal variation related to thermal tides, regional/local flows and other mesoscale variations, and turbulence. In addition, seasonal variations such as those produced by the CO_2 cycle are removed as well. An oscillation period of ~4.4 sols is observed both in wind and pressure data.

signal. As noted, other sol periods show more variability and weak peaks in the wind spectra that are usually not well correlated with pressure. This could be influenced by the data gaps in the Mars 2020 wind data. Given the gaps present in the data, it is expected that longer periods would also be affected by traveling waves.

6. Effects of the MY36/2022A Regional Dust Storm on the Surface Winds

An early RDS, developed from a local dust storm in the Hesperia–Promethei region (Malin & Cantor, 2022), affected Mars surface missions in January 2022 (MY36, L_s ~ 152°) expanding first to northward and after that eastward in the tropics of both hemispheres, passing over Jezero crater on 5 January on mission sol 313 (L_s ~ 153°). The MY36/2022A RDS increased opacity to values greater than 1.5 on sols 314–317 from pre-storm values lower than 0.5 and persisted with variable opacities until sol 319, the influence at Jezero lasting therefore six sols between L_s ~ 153° and ~ 156° (Lemmon et al., 2022). This event was the most intense observed by a surface mission since the MY34/2019 LDS that affected InSight's landing site at Elysium Planitia and MSL's landing site at Gale crater (Viúdez-Moreiras, Newman, et al., 2020). However, the MY36/2022A storm duration (six sols) was much shorter than the LDS duration (whose most noticeable disturbances ended a month after the first effects were observed, and high levels of dust remained in the atmosphere for several sols, see Figure 8 in Viúdez-Moreiras, Newman, et al. (2020)), more in agreement with the durations of typical RDSs. Pressure tides and near-surface temperatures were strongly affected at the Perseverance landing site, similar to what was observed during previous storms (e.g., Guzewich et al., 2016; Lewis & Barker, 2005; Ryan & Henry, 1979; Viúdez-Moreiras, Newman, et al., 2019, 2020; Wilson & Hamilton, 1996; Zurek & Leovy, 1981). However, Perseverance was the first mission to make meteorological observations at a location with active storm dust lifting; previous missions were either not located in active dust lifting centers, did not carry meteorological sensors, and/or could not operate during a storm due to being solar powered. This enabled Perseverance to study the strong aeolian activity (both dust lifting and sand motion) associated with the storm by the rover cameras and MEDA measurements, including the deposition of surface grains on the rover deck (Lemmon et al., 2022).

As described in Section 2, a close encounter with a DD on sol 313 at 13:42 further damaged WS2. Two sols later (sol 315 at 14:24), WS1 also experienced damage. The MEDA WS was unavailable to provide wind data. The WS was then kept off for several tens of sols, including over the remaining storm period. However, wind changes during the onset of the storm at Jezero were able to be measured.

Prior to the storm, on sols 310–311, the diurnal cycle of winds (Figure 10) was similar to that observed throughout the mission (Section 4) with the characteristic rotation between daytime and nighttime regimes consistent with slope flow control. Winds were east-southeasterlies during the daytime, peaking in the afternoon as usual, and then started to rotate progressively at ~17 hr toward westerlies. Between 20 and 21 hr, when winds were slowly rotating from upslope to downslope, strong winds developed with wind speeds compared to those measured in most of the daytime (but northerlies instead of the daytime's prevailing east-southeasterlies). This increase in wind speed after sunset was observed intermittently throughout the mission, but was more pronounced after sol ~300. By contrast, nighttime winds were weaker for sols 311–314 (Figure 10).

On sol 312, the effects of the dust storm were clearly observed in the wind data with southwesterlies between 10 and 11.5 hr rather than the usual southeasterlies observed, that is, the zonal winds were opposite in direction to those observed under nominal conditions (outside the dust storm). Winds abruptly rotated to southeasterlies at 11.5 hr and remained mostly as usual in the afternoon. On sol 313, the disturbances were more dramatic with a smooth clockwise rotation from southwesterlies to easterlies between 10 and ~14 hr and with stronger wind speeds than usual over this period, similar in magnitude to the peak speeds typically measured later in the afternoon. Due to the damage to WS2 at that time, which caused the WS to turn off for several sols, no wind data were taken during the afternoon under storm conditions; hence, the peak wind speeds during the storm may not

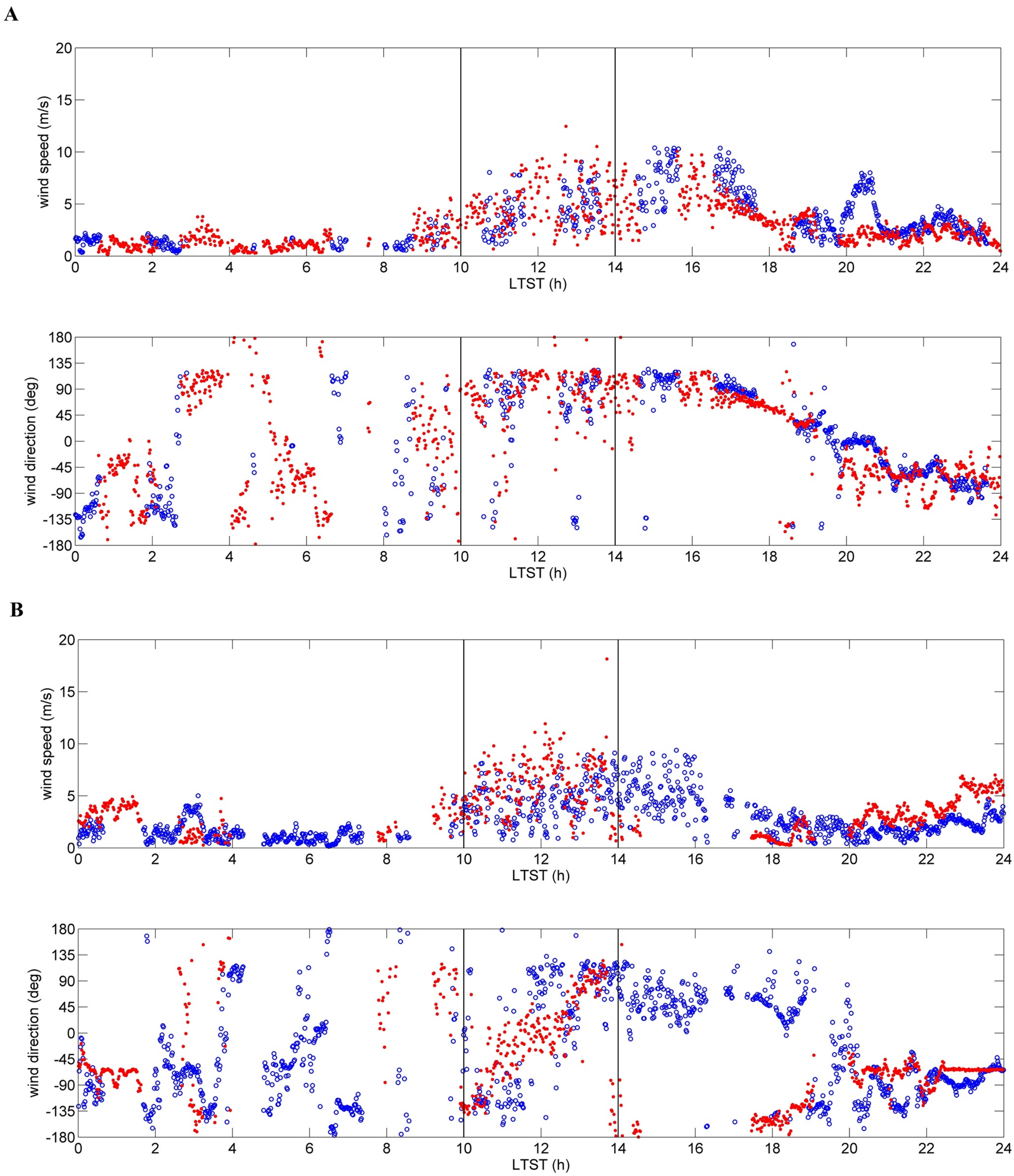

Figure 10. Wind speed and direction (1 min averages) for (a) sols 310 and 311 (pre-storm conditions; in blue and red, respectively) and (b) sols 312 and 313 (storm onset at Jezero; in blue and red, respectively). Vertical lines show 10:00 and 12:00 local true solar time (LTST) delimiting the period where the tidal flows were likely to produce the major change in winds during the storm. The direction from which the wind is blowing is shown, as in Figure 5, following the standard meteorological convention; although here in a [−180, 180] range to better visualize the wind rotation at sol 313.

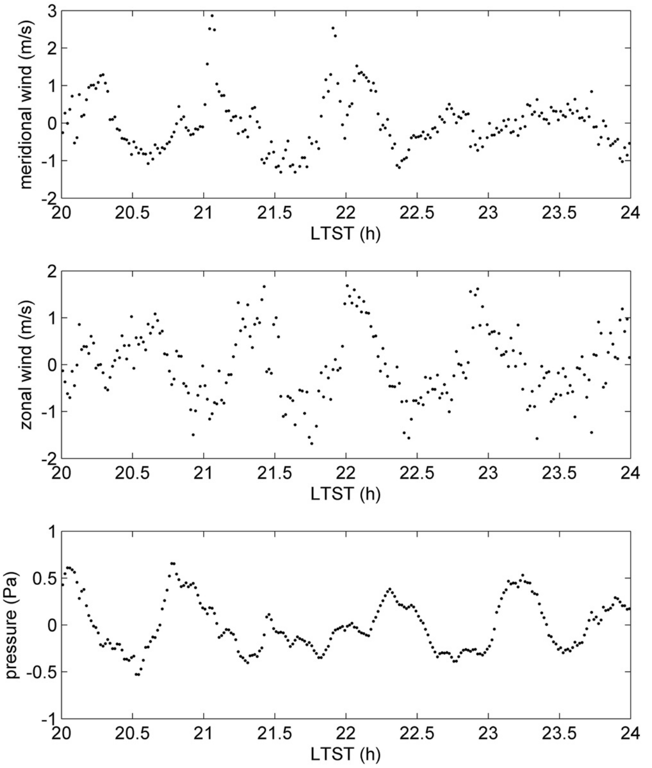

Figure 11. Waves observed at night during the regional dust storm, while downslope flows developed in Isidis basin and Jezero crater. Time evolution is shown as a function of local true solar time (LTST). Both pressure and wind were detrended subtracting a running average of $4{\cdot}10^3$ s from 1-min average signals.

have been captured. At night, the data extracted from the remaining operating boom (Viúdez-Moreiras et al., 2019a) suggested that downslope westerly flows were much more intense than under nominal conditions, reaching 7 ms^{-1} at midnight.

Changes to the surface wind pattern during a dust storm can arise from several different mechanisms, as discussed, for example, in Viúdez-Moreiras, Newman, et al. (2020). First, a dust storm can locally (or even regionally/globally) modify the atmospheric static stability (e.g., Zurek, 1976) and thus the coupling between winds aloft and near the surface. Second, once the dust storm has grown enough (this will also depend on its location) that it influences the large-scale pattern of solar heating, it can enhance the strength of the zonal mean meridional (Hadley cell) global circulation (Basu et al., 2006; Heavens et al., 2011; Kass et al., 2016). Third, and typically at the same stage of growth as in the latter case, it can increase the strength of thermal tides and thus tidal flows (e.g., Wilson & Hamilton, 1996; Zurek & Leovy, 1981). Indeed, such tidal enhancement has been linked to the broadening and strengthening of the summer solstice Hadley cell (Wilson & Hamilton, 1996). Additionally, the non-homogeneous dust content in the atmosphere could also provoke differential heating in the local scale; thus, pressure gradients leading to enhanced winds in dust fronts superimposed to the regional-to-large-scale phenomena described earlier.

At L_s 153°, the Hadley cell is transitioning from the solsticial southern winter cell to a weak, dual cell, equinoctial circulation. Simulations with the Mars-WRF GCM for $L_s \sim 153°$, presented in Figure 6, show, without the effects of a dust storm, surface winds fully driven by regional slope flows on the Jezero region in the Isidis basin slopes (the simulations do not resolve Jezero crater, which presents similar local slopes at Perseverance's location (W vs. NW), hence, a similar direction in the daytime anabatic winds). Simulations suggest that winds above the PBL are northwesterlies on average on the Isidis basin northwestern slopes throughout these sols, opposing the near-surface slope flows. These results are not consistent with dust storm observations, which suggest a mechanism producing high wind speeds instead of acting destructively. The observed clockwise rotation around noon from southwesterlies to easterlies between 10 and ~14 hr in sols 312 and 313 is also inconsistent with an enhanced Hadley cell circulation, which should promote a particular meridional component in surface winds, instead of variable northerlies or southerlies separated by a few hours. Also, the observed diurnal variation and the repeatability in different sols suggest that the origin of this perturbation is not local. Conversely, changes are in agreement with what is expected by thermal tides as was observed in previous storms. Thus, enhanced tidal flows likely affected the surface wind patterns at Jezero, producing a dramatic clockwise rotation from southwesterlies to easterlies around midday and in less than 4 hr. In fact, thermal tides were strongly affected during the dust storm. Both the diurnal and the semidiurnal pressure modes were doubled between sols 310 and 313, driving higher diurnal pressure amplitudes during this period. The changes included dramatic disturbances in phase as is usual during these events (e.g., Leovy & Zurek, 1979; Ryan & Henry, 1979; Zurek & Martin, 1993). The further deviation in the nominal wind patterns as diurnal and semidiurnal modes enhance and storm progresses supports this hypothesis.

The nighttime regime in sols 311–313, before the calm period, was affected by significant low-frequency oscillations (Figure 10), probably due to gravity waves. These oscillations were observed after the sunset, when downslope winds developed, and remained until midnight, with periods of 50 ± 10 min, and ~0.75 ± 0.25 m/s of amplitude in the zonal and meridional components of surface winds, with a small counterpart in pressure (~0.5 Pa) and temperature (~1 K) perturbations. Winds were, at that time, west-northwesterlies on sol 311, west-southwesterlies on sol 312, and west-northwesterlies on sol 313. Oscillations were better observed on sol 313 and in the zonal component of winds, likely as a result of the detrending procedure and the small relative uncertainties in the zonal component of surface winds (Figure 11). On that sol, there was an ~15 min shift in the zonal and meridional signals, that is, they were

~90° out of phase, while the phase difference between winds and pressure was ~180°. The relatively long period of these waves suggests that the origin is not local. Neglecting Coriolis forces and assuming a linear relationship between wind and pressure perturbations at the first order (Banfield et al., 2020; Coleman & Knupp, 2010), the phase speed, c, can be computed by $c = u + P'/(\rho \cdot u')$, where u is the wind speed, ρ is the atmospheric density, and P' and u' are the pressure and wind perturbations, respectively. It leads to phase speeds of 26–28 ms^{-1} and horizontal wavelengths of 70–90 km. Therefore, we suggest that the origin of these waves may be the slopes of Isidis basin, possibly due to topographical effects or wind shear between regional downslope winds and the general circulation disturbed by enhanced tidal flows. The enhancement of the wave activity during the MY36/2022A RDS at Jezero agrees with data from previous missions, which showed near-surface wave activity enhancement in dust storm periods (Banfield et al., 2020; Guzewich et al., 2021). Gravity waves have a strong relevance for atmospheric dynamics, including mixing of energy, momentum, and species in the very stable Martian nighttime PBL during dust storm conditions, as well as in the thermal structure of the atmosphere, and hence, in circulation (e.g., Barnes, 1980; Fritts & Alexander, 2003; Heavens et al., 2020 and references therein).

Sols 314 and 315, before the further damage to the WS, were mostly lost in terms of data, which were operating with only one working WS boom (pointing toward the front of the rover) and were a period when the rover heading was to the southwest, meaning that the remaining boom was unable to capture the prevailing daytime winds. However, the available data suggest that morning winds continued to be southwesterlies, as on sol 313, with maximum minute-averaged wind speeds close to 8 ms^{-1} in agreement with previous sols. Nighttime downslope winds appeared to develop on sol 314 as usual, although the available data prevent knowing if wave activity occurred as in previous sols.

Wind speeds deserve a special mention. Summarizing what was observed regarding wind speeds during the onset of the storm at Jezero, mean winds were slightly greater during the storm than in pre-storm conditions. On the other hand, vortex activity strongly increased during the storm, particularly in early stages (Lemmon et al., 2022) and provoked a higher probability of close encounters. One of these encounters at sol 313, 13:42, produced an intense wind gust reaching extreme wind speeds greater than 20 ms^{-1} that damaged the WS. This gust can be seen in Figure 10 in the two measurements that depart from the average on sol 313. The companion paper (part 2) will detail this event.

Given that no wind data are available after sol 315 (L_s 153°), there is no direct information on wind patterns after the storm. Model simulations predict similar behavior in near-surface wind patterns as the season progresses (Newman et al., 2021; Pla-García et al., 2020); they differ, in general, only in the strength of daytime and nighttime winds (with daytime winds being weaker in the northern winter). However, the modeled wind directions are mostly unaffected, showing easterly and south easterly winds at midday.

As described in Section 2, in the absence of a working WS, surface winds may be inferred, under particular conditions, from other sensors and/or from their interaction with surface. We have obtained some information on surface winds from DD Navcam surveys or movies after the WS damage. The wind direction estimations, acquired around noon local time or shifted to the afternoon, are presented in Table 2. It was possible to infer the DD trajectory in 25 events from sol 323 (L_s 158°) to sol 563 (L_s 306°). The only reported events to have well-constrained distance and radial motion were on sol 425, 472, and 537: the first, shown in Figure 12, was a 32 ± 3 m diameter DD moving WSW, 300 ± 20 m away, at 5.2 ± 0.5 $m \cdot s^{-1}$; the second was a 20–40 m length gust on sol 472 moving WNW at 14 ± 4 $m \cdot s^{-1}$, and the third was an ~30 m diameter DD moving WNW at 13 ± 3 $m \cdot s^{-1}$ from a distance of 1.5 km in the first set of images, ending 780 m away. The surveys showed diurnal wind directions that are consistent with the MEDA data before sol 313 and with the model simulations. On average, inferred wind directions were southeasterlies around the fall equinox and easterlies between the equinox and the winter solstice, with significant deviations probably due to the daytime turbulence, mainly around the fall equinox. These observational data strongly suggest that prevailing winds continued to be slope-driven even in northern winter. Additionally, it is likely that the topography affected the background wind patterns as the rover approached the delta walls (Section 3). It opens the possibility of expanding our knowledge of surface wind patterns with other wind indicators as the mission progresses, thus complementing the WS data.

Table 2
Inferred Wind Direction From Dust Lifting Events Detected in Navcam Surveys or Movies

Mission sol	L_s (°)	LMST (hr)	Event notes	Inferred background wind direction (°)
323	158	12:50		90 ± 30
327	160	12:33		135 ± 15
347	171	12:42	The apparent motion is slight toward 305 with wobbling	125 ± 15
362	180	15:38		100 ± 20
364	181	12:20	Slight movement	160 ± 30
365	181	13:08		135 ± 45
368	183	12:04		90 ± 45
370	184	11:37	Dust devils seem to converge and get closer	10 ± 15
372	185	11:40	Multiple dust devils move away from rover	10 ± 15
373	186	11:56		180 ± 30
373	186	11:58	Slight movement	150 ± 15
380	190	15:50	Very distant dust devils	Indeterminate
383	192	11:40	Very distant dust devils	Indeterminate
407	207	15:00	Sense of movement is uncertain	60 ± 30 or 240 ± 30
425	218	13:40	Nearby DD	65 ± 15
472	248	12:25	Distant dust devil and nearby dust cloud move toward rover	120 ± 15
473	249	12:07	Two distant dust devils converge	120 ± 15
484	256	12:35		90 ± 30
508	271	11:54		90 ± 45
514	275	13:54		90 ± 45
519	278	13:12	Very distant	90 ± 60
519	278	13:26	Motion inconsistent between 2	90 ± 45
521	280	12:56		90 ± 45
528	284	12:31		130 ± 15
537	290	15:05	~30 m wide, moving at 13 ± 3 $m \cdot s^{-1}$	135 ± 30
540	292	13:58		90 ± 45
563	306	13:44		135 ± 45

Note. Mission sol, areocentric solar longitude (L_s), local mean solar time (LMST), and event notes are included together with the inferred background wind direction. The direction from which the wind is blowing is shown, following the standard meteorological convention.

7. Summary and Conclusions

This paper presents the observed wind patterns at Perseverance's landing site, on the Jezero crater floor close to the delta of an ancient river. The contemporaneous wind measurements in Jezero have also supported the first flights of an unmanned aerial vehicle, the Ingenuity helicopter, on Mars.

The observed wind patterns at Jezero presented minor sol-to-sol variations generally overwhelmed by diurnal variations in accordance with observations by previous missions on Mars outside the dust storm season. No significant variability was observed in the general shape of the diurnal cycle during the observation period. Conversely, a mostly repeatable diurnal cycle was measured and presented two regimes: (a) a daytime or convective regime, from dawn to sunset, with average easterly to southeasterly winds and where maximum wind speeds were measured, and (b) a nighttime regime with a period of westerly/northwesterly winds followed by a period of relative calm until sunrise with highly variable wind directions as a function of sol and time of night. The timing and magnitude of the observed regimes are consistent with control by slope flows.

The fact that the slopes of Isidis basin and the Jezero crater western rim have a nearly similar direction complicates the discernment of which mechanism is modulating the diurnal cycle at the landing site. During the daytime,

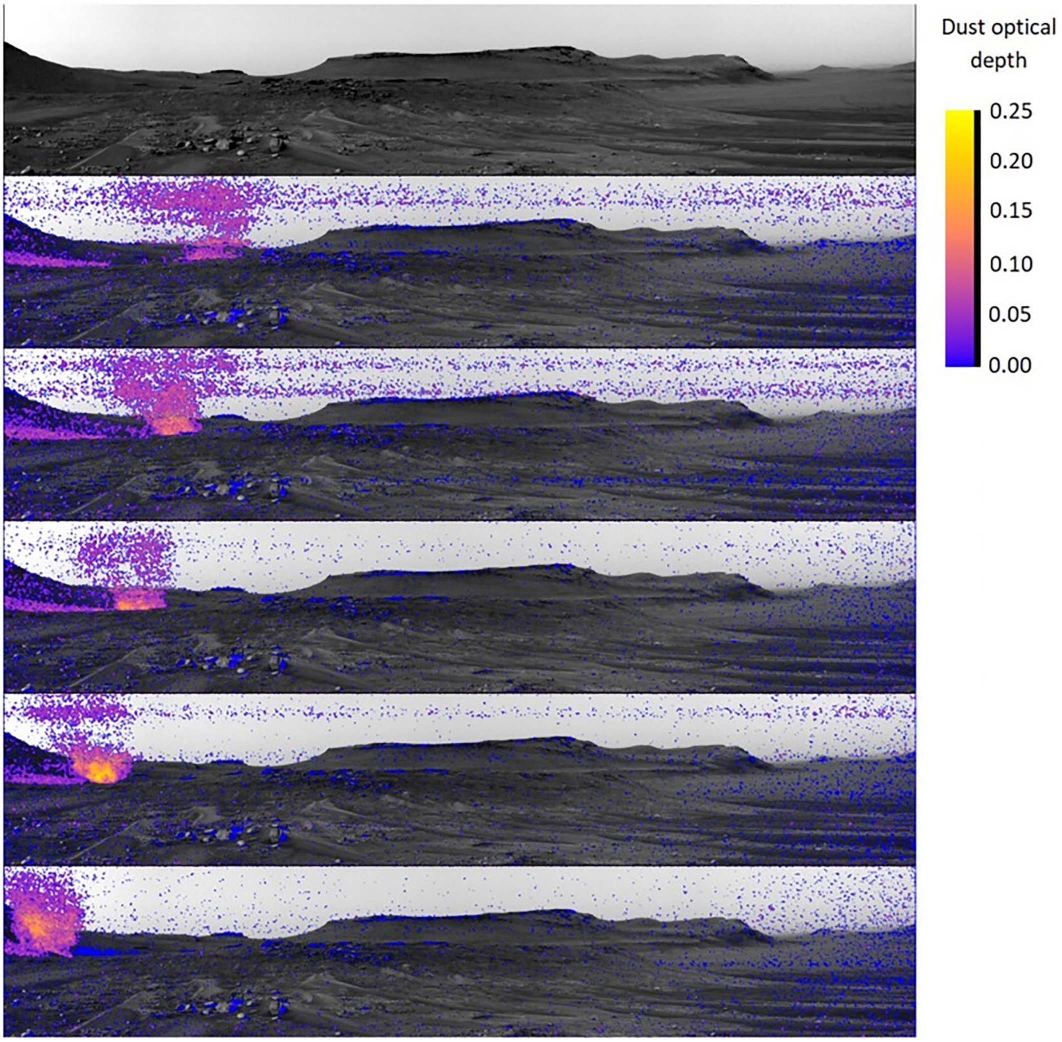

Figure 12. Enhanced color images for the event at sol 425, corresponding with a dust devil moving WSW, 300 ± 20 m away the rover, at 5.2 ± 0.5 m/s. Dust optical depth is included. Delta walls are likely affecting background winds at that location (see text).

the gradual increase in wind speeds and the shift in wind direction as the daytime timeslot progressed can be interpreted as the result of the gradual and different increase in the relative strength of regional and local slope flows. During the night, the thin PBL depth maximizes the effect of smaller topographic features near the rover, therefore affecting the intensity of the regional-scale downslope winds in these areas, promoting local flows and increasing mechanical turbulence. The Jezero region and the crater itself present significant topography that could dramatically affect the nighttime patterns in the mesoscale and in the microscale. The first part of the night, from sunset to ∼01 hr, was characterized by quite stable westerly/northwesterly winds, peaking around midnight as a likely result of downslope winds peaking at that time, which is reproduced by pre-landing simulations (Newman et al., 2021). After ∼01 hr, winds decreased in intensity and rotated counterclockwise to roughly easterlies with a dramatic variability during most of the nighttime. This reduction in the relative intensity of the crater rim downslope winds at the rover's location would enhance the effect of competing mechanisms, likely downslope winds at the eastern crater rim reinforced by downslope flows on M01-SE. The great sub-diurnal and sol-to-sol variability observed by Mars 2020 was consistent with an increase in mechanical turbulence caused by these convergent flows on the crater floor. The very low wind speeds observed during the early morning suggests that these flows were very weak and/or that a destructive interaction around the landing site was dominating the atmospheric dynamics, inducing a calm region on the crater floor.

Data suggest that the surface circulation at Jezero in northern spring and summer is highly unaffected by large-scale circulation, except during particular periods in the diurnal cycle, or more generally, during dust storms conditions. As a result, the seasonal variability for the winds in the period observed by Mars 2020 between the northern spring and the summer season was weak without dramatic variations. However, sol-to-sol and seasonal effects were observed by Perseverance rover, most of them at periods during the night. One of these particular periods in the diurnal cycle is the transition from daytime to nighttime. In the first sols of the mission, the transition from daytime to nighttime wind directions involved a counterclockwise rotation, but this reversed to a clockwise rotation as the mission progressed. The duration of the transition was also long close to the equinoxes, lasting several hours, and sharp around the summer solstice. This seasonal behavior in the transition between upslope and downslope winds could be related to a coupled effect of Hadley cell return flow and thermal tides. Between 20 and 21 hr, when winds were slowly rotating from upslope to downslope, strong winds developed in some sols, producing wind speeds comparable in some cases to those measured in most of the daytime, but with different directions from the prevailing southeasterlies. Also, nighttime downslope flows lasted variable durations. After peaking at midnight, they intermittently reached Perseverance's location in some sols of the mission, and in others, the calm period was present earlier. During this nighttime period and in early morning, seasonal variations suggest large-scale interactions with the regional and local circulation. The influence by large-scale circulation may be greater in northern winter, when the mean meridional circulation is on its strongest.

Although the sol-to-sol variations were weak on average, traveling wave activity was observed in surface winds at Jezero. A strong peak appeared between sols 130 and 170, corresponding to waves of 4.4 sol period and $\sim$0.5 ms^{-1} of amplitude in wind speed. Given the gaps present on the Mars 2020 wind data, it is expected that longer periods would also be affected by baroclinic instability.

An early RDS (MY36/2022A) affected Mars on January 2022 ($L_s \sim 153°$). The optical depth in Jezero crater showed significant effects on sol 313. A close encounter with a DD on this sol damaged the WS, and further damage on sol 315 meant that no wind data are available for the remaining storm period. However, the onset of the storm at Jezero was captured and showed dramatic perturbations in wind directions compatible with tidal flows produced by enhanced thermal tides, and increased wind speeds both during day and night. The nighttime regime on sols 311–313 was affected by significant low-frequency oscillations, suspected to be from gravity waves. Given our estimated horizontal wavelengths and that these waves were observed at nighttime, we suggest that their origin is not local. The origin of these waves may be the slopes of Isidis basin, which is the nearest feature with topography of similar horizontal scale. The enhancement of wave activity during the RDS at Jezero agrees with results of previous missions and is highly relevant for atmospheric dynamics, including mixing of energy, momentum, and species in the nighttime PBL during dust storm conditions.

There are no wind data after the storm at L_s 153°. In the absence of a working WS, surface winds may be inferred, under particular conditions, from other sensors and/or from their interaction with surface. We have obtained some information on surface winds from DD movies taken by the rover's cameras. On average, inferred wind directions were southeasterlies around the fall equinox and easterlies between the equinox and the winter solstice. These observational data strongly suggest that prevailing winds continued to be slope-driven during the late summer, fall, and early winter seasons, opening the possibility of extending the wind data set with other wind indicators as the mission progresses. Additionally, it is likely that the topography affected the background wind patterns as the rover approached the delta walls.

Acknowledgments

The authors acknowledge and thank the Mars 2020 team. The authors would like to thank Editors and two anonymous reviewers for their constructive reviews, which greatly improved this manuscript. This work was supported by the Spanish Ministry of Science and Innovation, under project RTI2018-098728-B-C31. The derived data presented in this work were processed in the DPS24PA system, which is supported by project no. DV2020-ATM-A01. Part of the research was carried out at the Jet Propulsion Laboratory, California Institute of Technology, under a contract with the National Aeronautics and Space Administration (80NM0018D0004). The UPV/EHU team was supported by Grant PID2019-109467GB-I00 funded by 1042 MCIN/AEI/10.13039/501100011033 and by Grupos Gobierno Vasco IT1742-22.

Data Availability Statement

The derived data used for generating the figures displayed in this article are available on Mendeley Data (Viudez-Moreiras, 2022). Other calibrated and derived Perseverance data used in this work are publicly available in the NASA's Planetary Data System (Rodriguez-Manfredi & de la Torre Juarez, 2021). The orbital data used in this work are publicly available via the NASA's Planetary Data System (McEwen, 2007; Neumann et al., 2003).

References

Balaram, J., Aung, M., & Golombek, M. P. (2021). The ingenuity helicopter on the perseverance rover. *Space Science Reviews*, *217*(4), 56. https://doi.org/10.1007/s11214-021-00815-w

Balme, M., & Greeley, R. (2006). Dust devils on Earth and Mars. *Reviews of Geophysics*, *44*(3), RG3003. https://doi.org/10.1029/2005RG000188

Banfield, D., Spiga, A., Newman, C., Forget, F., Lemmon, M., Lorenz, R., et al. (2020). The atmosphere of Mars as observed by InSight. *Nature Geoscience*, *13*(3), 190–198. https://doi.org/10.1038/s41561-020-0534-0

Barnes, J. R. (1980). Time spectral analysis of midlatitude disturbances in the Martian atmosphere. *Journal of the Atmospheric Sciences*, *37*(9), 2002–2015. https://doi.org/10.1175/1520-0469(1980)037<2002:tsaomd>2.0.co;2

Barnes, J. R. (1984). Linear baroclinic instability in the Martian atmosphere. *Journal of the Atmospheric Sciences*, *41*(9), 1536–1550. https://doi.org/10.1175/1520-0469(1984)041<1536:lbiitm>2.0.co;2

Basu, S., Wilson, J., Richardson, M., & Ingersoll, A. (2006). Simulation of spontaneous and variable global dust storms with the GFDL Mars GCM. *Journal of Geophysical Research*, *111*, E09004. https://doi.org/10.1029/2005JE002660

Battalio, J. M. (2021). Baroclinic traveling waves detected by Mars 2020 MEDA. In *AGU Fall Meeting 2021, held in New Orleans, LA, 13–17 December 2021, Abstract P25A-01*.

Bell, J. F., Maki, J. N., Alwmark, S., Ehlmann, B. L., Fagents, S. A., Grotzinger, J. P., et al. (2022). Geological, multispectral, and meteorological imaging results from the Mars 2020 Perseverance rover in Jezero crater. *Science Advances*, *8*(47). https://doi.org/10.1126/sciadv.abo4856

Charalambous, C., McClean, J. B., Baker, M., Pike, W. T., Golombek, M., Lemmon, M., et al. (2021). Vortex-dominated aeolian activity at InSight's landing site, Part 1: Multi-instrument observations, analysis and implications. *Journal of Geophysical Research*, *126*(6), e2020JE006757. https://doi.org/10.1029/2020JE006757

Coleman, T. A., & Knupp, K. R. (2010). A nonlinear impedance relation for the surface winds in pressure disturbances. *Journal of the Atmospheric Sciences*, *67*(10), 3409–3422. https://doi.org/10.1175/2010jas3457.1

Day, M., & Dorn, T. (2019). Wind in Jezero crater, Mars. *Geophysical Research Letters*, *46*(6), 3099–3107. https://doi.org/10.1029/2019gl082218

Etiope, G., & Oehler, D. Z. (2019). Methane spikes, background seasonality and non-detections on Mars: A geological perspective. *Planetary and Space Science*, *168*, 52–61. https://doi.org/10.1016/j.pss.2019.02.001

Farley, K. A., Williford, K. H., Stack, K. M., Bhartia, R., Chen, A., dela Torre, M., et al. (2020). Mars 2020 mission overview. *Space Science Reviews*, *216*(8), 142. https://doi.org/10.1007/s11214-020-00762-y

Fritts, D. C., & Alexander, M. J. (2003). Gravity wave dynamics and effects in the middle atmosphere. *Reviews of Geophysics*, *41*(1), 1003. https://doi.org/10.1029/2001rg000106

Gomez-Elvira, J., Armiens, C., Castaner, L., Dominguez, M., Genzer, M., Gomez, F., et al. (2012). REMS: The environmental sensor suite for the Mars Science Laboratory rover. *Space Science Reviews*, *170*(1–4), 583–640. https://doi.org/10.1007/s11214-012-9921-1

Greeley, R., Whelley, P. L., Arvidson, R. E., Cabrol, N. A., Foley, D. J., Franklin, B. J., et al. (2006). Active dust devils in Gusev crater, Mars: Observations from the Mars exploration rover, spirit. *Journal of Geophysical Research*, *111*(E12), E12S09. https://doi.org/10.1029/2006JE002743

Guzewich, S., de la Torre-Juárez, M., Newman, C. E., Mason, E., Smith, M. D., Miller, N., et al. (2021). Gravity wave observations by the Mars Science Laboratory REMS pressure sensor and comparison with mesoscale atmospheric modeling with MarsWRF. *Journal of Geophysical Research: Planets*, *126*(8), e2021JE006907. https://doi.org/10.1029/2021je006907

Guzewich, S., Newman, C. E., de la Torre Juarez, M., Wilson, R. J., Lemmon, M., Smith, M. D., et al. (2016). Atmospheric tides in Gale crater, Mars. *Icarus*, *268*, 37–49. https://doi.org/10.1016/j.icarus.2015.12.028

Heavens, N. G., Kass, D. M., Kleinbohl, A., & Schofield, J. T. (2020). A multiannual record of gravity wave activity in Mars's lower atmosphere from on-planet observations by the Mars Climate Sounder. *Journal of Geophysical Research*, *341*, 113630. https://doi.org/10.1016/j.icarus.2020.113630

Heavens, N. G., McCleese, D. J., Richardson, M. I., Kass, D. M., Kleinböhl, A., & Schofield, J. T. (2011). Structure and dynamics of the Martian lower and middle atmosphere as observed by the Mars climate sounder: 2. Implications of the thermal structure and aerosol distributions for the mean meridional circulation. *Journal of Geophysical Research*, *116*(E1), E01010. https://doi.org/10.1029/2010JE003713

Hess, S. L., Henry, R. M., Leovy, C. B., Ryan, J. A., & Tillman, J. E. (1977). Meteorological results from the surface of Mars: Viking 1 and 2. *Journal of Geophysical Research*, *82*(28), 4559–4574. https://doi.org/10.1029/js082i028p04559

Holstein-Rathlou, C., Gunnlaugsson, H. P., Merrison, J. P., Bean, K. M., Cantor, B. A., Davis, J. A., et al. (2010). Winds at the Phoenix landing site. *Journal of Geophysical Research*, *115*, E00E18. https://doi.org/10.1029/2009JE003411

Kahanpää, H., & Viúdez-Moreiras, D. (2021). Modelling Martian dust devils using in-situ wind, pressure, and UV radiation measurements by Mars Science Laboratory. *Icarus*, *359*, 114207. https://doi.org/10.1016/j.icarus.2020.114207

Kass, D. M., Kleinböhl, A., McCleese, D. J., Schofield, J. T., & Smith, M. D. (2016). Interannual similarity in the Martian atmosphere during the dust storm season. *Geophysical Research Letters*, *43*(12), 6111–6118. https://doi.org/10.1002/2016gl068978

Lemmon, M. T., Smith, M. D., Viudez-Moreiras, D., de la Torre-Juarez, M., Vicente-Retortillo, A., Munguira, A., et al. (2022). Dust, sand, and winds within an active Martian storm in Jezero crater. *Geophysical Research Letters*, *49*, e2022GL100126. https://doi.org/10.1029/2022GL100126

Leovy, C. B., & Zurek, R. W. (1979). Thermal tides and Martian dust storms: Direct evidence for coupling. *Journal of Geophysical Research*, *84*(B6), 2956–2968. https://doi.org/10.1029/JB084iB06p029

Lewis, S. R., & Barker, P. R. (2005). Atmospheric tides in a Mars general circulation model with data assimilation. *Advances in Space Research*, *36*(11), 2162–2168. https://doi.org/10.1016/j.asr.2005.05.122

Malin, M. C., & Cantor, B. A. (2022). MRO MARCI Weather Report for the week of 3 January 2022–9 January 2022 (Malin Space Science Systems Captioned Image Release, MSSS-604). Retrieved from http://www.msss.com/msss_images/2022/01/12/

McEwen, A. (2007). *Mars reconnaissance orbiter high resolution imaging science experiment* (Reduced Data Record, MRO-M-HIRISE-3-RDR-V1.1). NASA Planetary Data System.

Mischna, M., Richardson, M., Grip, H., Balaram, J., Aung, M., Cantor, B., et al. (2021). Atmospheric assessment in support of ingenuity helicopter flights. In *AGU Fall Meeting 2021, held in New Orleans, LA, 13–17 December 2021, Abstract P25I-2247*.

Mitchell, D. M., Montabone, L., Thomson, S., & Read, P. L. (2015). Polar vortices on Earth and Mars: A comparative study of the climatology and variability from reanalyses. *Quarterly Journal of the Royal Meteorological Society*, *141*(687), 550–562. https://doi.org/10.1002/qj.2376

Montabone, L., Spiga, A., Kass, D. M., Kleinboehl, A., Forget, F., & Millour, E. (2020). Martian year 34 column dust climatology from Mars climate sounder observations: Reconstructed maps and model simulations. *Journal of Geophysical Research: Planets*, *125*(8), e2019JE006111. https://doi.org/10.1029/2019je006111

Murphy, J. R., Leovy, C. B., & Tillman, J. E. (1990). Observations of Martian surface winds at the Viking Lander 1 site. *Journal of Geophysical Research*, *95*(B9), 14555–14576. https://doi.org/10.1029/jb095ib09p14555

Neumann, G., Zuber, M., & Smith, D. E. (2003). MOLA mission experiment gridded data recor [Dataset]. NASA Planetary Data System. https://doi.org/10.17189/1519460

Newman, C. E., de la Torre, M., Pla-García, J., Wilson, R. J., Lewis, S. R., Neary, L., et al. (2021). Multi-model meteorological and aeolian predictions for Mars 2020 and the Jezero Crater Region. *Space Science Reviews*, *217*(1), 1–68. https://doi.org/10.1007/s11214-020-00788-2

Newman, C. E., Hueso, R., Lemmon, M. T., Munguira, A., Vicente-Retortillo, Á., Apestigue, V., et al. (2022). The dynamic atmospheric and aeolian environment of Jezero crater, Mars. *Science Advances*, *8*(21), eabn3783. https://doi.org/10.1126/sciadv.abn3783

Newman, C. E., Gómez-Elvira, J., Marín, M., Navarro, S., Torres, J., Richardson, M. I., et al. (2017). Winds measured by the Rover Environmental Monitoring Station (REMS) during the Mars Science Laboratory (MSL) rover's Bagnold Dunes campaign and comparison with numerical modeling using MarsWRF. *Icarus*, *291*, 203–231. https://doi.org/10.1016/j.icarus.2016.12.016

Pla-García, J., Munguira, A., Rafkin, S. C., Hueso, R., Sánchez-Lavega, A., de la Torre, M., et al. (2022). Nocturnal turbulence at Jezero driven by the onset of a low-level jet as determined from MRAMS modeling and MEDA measurements. In *Seventh international workshop on the Mars atmosphere: Modelling and observations, held in Paris, France, 14–17 June 2022*.

Pla-García, J., Rafkin, S., Martinez, G., de Vicente, A., Newman, C., Savijarvi, H., et al. (2020). Meteorological predictions for Mars 2020 Perseverance Rover landing site at Jezero crater. *Space Science Reviews*, *216*(8), 1–21. https://doi.org/10.1007/s11214-020-00763-x

Pla-Garcia, J., Rafkin, S. C. R., Kahre, M., Gomez-Elvira, J., Hamilton, V. E., Navarro, S., et al. (2016). The meteorology of Gale crater as determined from rover environmental monitoring station observations and numerical modeling. Part I: Comparison of model simulations with observations. *Icarus*, *280*, 103–113. https://doi.org/10.1016/j.icarus.2016.03.013

Rafkin, S. C., Pla-Garcia, J., Kahre, M., Gomez-Elvira, J., Hamilton, V. E., Marín, M., et al. (2016). The meteorology of Gale Crater as determined from rover environmental monitoring station observations and numerical modeling. Part II: Interpretation. *Icarus*, *280*, 114–138. https://doi.org/10.1016/j.icarus.2016.01.031

Reiss, D., Spiga, A., & Erkeling, G. (2014). The horizontal motion of dust devils on Mars derived from CRISM and CTX/HiRISE observations. *Icarus*, *227*, 8–20. https://doi.org/10.1016/j.icarus.2013.08.028

Richardson, M. I., & Newman, C. E. (2018). On the relationship between surface pressure, terrain elevation, and air temperature. Part I: The large diurnal surface pressure range at Gale Crater, Mars and its origin due to lateral hydrostatic adjustment. *Planetary and Space Science*, *164*, 132–157. https://doi.org/10.1016/j.pss.2018.07.003

Richardson, M. I., & Wilson, R. (2002). A topographically forced asymmetry in the Martian circulation and climate. *Nature*, *416*(6878), 298–301. https://doi.org/10.1038/416298a

Rodriguez-Manfredi, J. A., & de la Torre Juarez, M. (2021). Mars 2020 perseverance rover Mars environmental dynamics analyzer (MEDA) experiment data record (EDR) and reduced data record (RDR) data products archive bundle. *PDS Atmospheres Node*, *10*, 1522849. https://doi.org/10.17189/1522849

Rodríguez-Manfredi, J. A., de la Torre Juárez, M., Alonso, A., Apéstigue, V., Arruego, I., Atienza, T., et al. (2021). The Mars Environmental Dynamics Analyzer, MEDA. A suite of environmental sensors for the Mars 2020 mission. *Space Science Reviews*, *217*, 1–86. https://doi.org/10.1007/s11214-021-00816-9

Ryan, J. A., & Henry, R. M. (1979). Mars atmospheric phenomena during major dust storms, as measured at surface. *Journal of Geophysical Research*, *84*(B6), 2821–2829. https://doi.org/10.1029/JB084iB06p02821

Ryan, J. A., Henry, R. M., Hess, S. L., Leovy, C. B., Tillman, J. E., & Walcek, C. (1978). Mars meteorology: Three seasons at the surface. *Geophysical Research Letters*, *5*(8), 715–718. https://doi.org/10.1029/gl005i008p00715

Sánchez-Lavega, A., Rio-Gaztelurrutia, T. d., Hueso, R., Juárez, M. d. l. T., Martínez, G. M., Harri, A.-M., et al. (2022). Mars 2020 Perseverance rover studies of the Martian atmosphere over Jezero from pressure measurements. *Journal of Geophysical Research: Planets*, *127*, e2022JE007480. https://doi.org/10.1029/2022JE007480

Schieber, J., Minitti, M. E., Sullivan, R., Edgett, K. S., Malin, M. C., Parker, T., & Calef, F. (2020). Engraved on the rocks—Aeolian abrasion of Martian mudstone exposures and their relationship to modern wind patterns in Gale Crater, Mars. *The Depositional Record*, *6*(3), 625–647. https://doi.org/10.1002/dep2.110

Schon, S., Head, J. W., & Fassett, C. I. (2012). An overfilled lacustrine system and progradational delta in Jezero crater, Mars: Implications for Noachian climate. *Planetary and Space Science*, *67*(1), 28–45. https://doi.org/10.1016/j.pss.2012.02.003

Spiga, A., Murdoch, N., Lorenz, R., Forget, F., Newman, C., Rodriguez, S., et al. (2021). A study of daytime convective vortices and turbulence in the Martian planetary boundary layer based on half-a-year of InSight atmospheric measurements and large-eddy simulations. *Journal of Geophysical Research: Planets*, *126*(1), e2020JE006511. https://doi.org/10.1029/2020je006511

Stanzel, C., Pätzold, M., Williams, D. A., Whelley, P. L., Greeley, R., Neukum, G., & HRSC Co-Investigator Team. (2008). Dust devil speeds, directions of motion and general characteristics observed by the Mars Express High Resolution Stereo Camera. *Icarus*, *197*(1), 39–51. https://doi.org/10.1016/j.icarus.2008.04.017

Sullivan, R., Golombek, M., Wilson, G., Greeley, R., Kraft, M., Herkenhoff, K., et al. (2000). Results of the imager for Mars Pathfinder windsock experiment. *Journal of Geophysical Research*, *105*(E10), 24547–24562. https://doi.org/10.1029/1999je001234

Sullivan, R., & Kok, J. F. (2017). Aeolian saltation on Mars at low wind speeds. *Journal of Geophysical Research: Planets*, *122*(10), 2111–2143. https://doi.org/10.1002/2017JE005275

Tyler, D., Jr., & Barnes, J. R. (2013). Mesoscale modeling of the circulation in the Gale Crater region: An investigation into the complex forcing of convective boundary layer depths. *International Journal of Mars Science and Exploration*, *8*, 58–77. https://doi.org/10.1555/mars.2013.0003

Vasavada, A. (2022). Mission overview and scientific contributions from the Mars Science Laboratory Curiosity rover after eight years of surface operations. *Space Science Reviews*, *218*(3), 14. https://doi.org/10.1007/s11214-022-00882-7

Viúdez-Moreiras, D. (2021). A three-dimensional atmospheric Dispersion model for Mars. *Progress in Earth and Planetary Science*, *8*(53), 53. https://doi.org/10.1186/s40645-021-00445-4

Viudez-Moreiras, D. (2022). Supporting material – Viudez-Moreiras et al. (2022a, 2022b; Journal of Geophysical Research: Planets), Mendeley Data, V1. https://doi.org/10.17632/v6hght8rfb.1

Viúdez-Moreiras, D., Arvidson, R. E., Gómez-Elvira, J., Webster, C., Newman, C. E., Mahaffy, P., & Vasavada, A. R. (2020). Advective fluxes in the Martian regolith as a mechanism driving methane and other trace gas emissions to the atmosphere. *Geophysical Research Letters*, *47*(3), e2019GL085694. https://doi.org/10.1029/2019gl085694

Viúdez-Moreiras, D., de la Torre, M., Gómez-Elvira, J., Lorenz, R. D., Apéstigue, V., Guzewich, S., et al. (2022). Winds at the Mars 2020 landing site. Part 2: Wind variability and turbulence. *Journal of Geophysical Research: Planets*, *127*, e2022JE007523. https://doi.org/10.1029/2022JE007523

Viúdez-Moreiras, D., Gómez-Elvira, J., Newman, C. E., Navarro, S., Marin, M., Torres, J., et al. (2019a). Gale surface wind characterization based on the Mars Science Laboratory REMS dataset. Part I: Wind retrieval and Gale's wind speeds and directions. *Icarus*, *319*, 909–925. https://doi.org/10.1016/j.icarus.2018.10.011

Viúdez-Moreiras, D., Gómez-Elvira, J., Newman, C. E., Navarro, S., Marin, M., Torres, J., et al. (2019b). Gale surface wind characterization based on the Mars Science Laboratory REMS dataset. Part II: Wind probability distributions. *Icarus*, *319*, 645–656. https://doi.org/10.1016/j.icarus.2018.10.010

Viúdez-Moreiras, D., Newman, C. E., de la Torre, M., Martinez, G., Guzewich, S., Lemmon, M., et al. (2019). Effects of the MY34/2018 global dust storm as measured by MSL REMS in Gale Crater. *Journal of Geophysical Research: Planets*, *124*(7), 1899–1912. https://doi.org/10.1029/2019JE005985

Viúdez-Moreiras, D., Newman, C. E., Forget, F., Lemmon, M., Banfield, D., Spiga, A., et al. (2020). Effects of a large dust storm in the near-surface atmosphere as measured by InSight in Elysium Planitia, Mars. Comparison with contemporaneous measurements by Mars Science Laboratory. *Journal of Geophysical Research: Planets*, *125*(9), e2020JE006493. https://doi.org/10.1029/2020JE006493

Viúdez-Moreiras, D., Richardson, M. I., & Newman, C. E. (2021). Constraints on Emission source locations of methane detected by Mars Science Laboratory. *Journal of Geophysical Research: Planets*, *126*(12), e2021JE006958. https://doi.org/10.1029/2021JE006958

Webster, C. R., Mahaffy, P. R., Atreya, S. K., Moores, J. E., Flesch, G. J., Malespin, C., et al. (2018). Background levels of methane in Mars' atmosphere show strong seasonal variations. *Science*, *360*(6393), 1093–1096. https://doi.org/10.1126/science.aaq0131

Wilson, R. J., & Hamilton, K. P. (1996). Comprehensive model simulation of thermal tides in the Martian atmosphere. *Journal of the Atmospheric Sciences*, *53*(9), 1290–1326. https://doi.org/10.1175/1520-0469(1996)053<1290:cmsott>2.0.co;2

Zurek, R. W. (1976). Diurnal tide in the Martian atmosphere. *Journal of the Atmospheric Sciences*, *33*(2), 321–337. https://doi.org/10.1175/1520-0469(1976)033<0321:dtitma>2.0.co;2

Zurek, R. W., & Leovy, C. B. (1981). Thermal tides in the dusty Martian atmosphere: A verification of theory. *Science*, *213*(4506), 437–439. https://doi.org/10.1126/science.213.4506.437

Zurek, R. W., & Martin, L. J. (1993). Interannual variability of planet-encircling dust storms on Mars. *Journal of Geophysical Research*, *98*(E2), 3247–3259. https://doi.org/10.1029/92je02936